Cooperative effects of surface plasmon resonance and type-II band alignment to significantly boost photoelectrochemical H_2 generation of TiO_2/CdS/TiN nanorod array photoanode

Jianan Li, Lijuan Wang [*], Wenzhong Wang, Xinglin Jia, Yuanyuan Zhang, Hang Yang, Yujie Li, Qing Zhou [*]

School of Science, Minzu University of China, Beijing 100081, PR China

ARTICLE INFO

ABSTRACT

Here, we demonstrate for the first time a novel ternary TiO_2/CdS/TiN nanorod array (NRA) photoanode for high-efficiency photoelectrochemical H_2 generation under bias-free simulated sunlight illumination. The ternary photoanode was constructed through modifying TiO_2 nanorod arrays with two-dimensional (2D) CdS nanosheets and nonmetal plasmonic TiN nanoparticles. In this novel photoanode, 2D CdS nanosheets with large surface area not only improve visible light absorption, but also extend the contact area with TiO_2 to form type-II band structure favorable for the separation and transfer of photogenerated electron-hole pairs. Moreover, 2D CdS nanosheets provide more sites to absorb TiN nanoparticles to further boost photon energy utilization via surface plasmon resonance-induced hot electron injection. The TiO_2/CdS/TiN NRA photoanode achieved an average H_2 generation rate of 129.6 $\mu mol\ cm^{-2}\ h^{-1}$, 4.2 times that of TiO_2 NRA photoanode. Substantially boosted photoelectrochemical H_2 generation of the TiO_2/CdS/TiN NRA photoanode is attributed to effective hot-electron injection and charge separation.

1. Introduction

Developing the technologies to generate renewable energy in a low-budget and eco-friendly way is great of very importance due to the growing energy demands and environmental contamination [1,2]. Among the developed approaches, photoelectrochemical (PEC) water splitting technology has attracted increasingly concern in directly converting the low-density solar energy into the high-density chemical fuels without any carbon emission [3,4]. Hitherto, numerous semiconductor oxides including TiO_2 [5], ZnO [6], WO_3 [7], $BiVO_4$ [8,9] and Bi_2MoO_6 [10] have been adopted as photoanode materials to split water into chemical fuels through PEC cell. As reported previously, wide band-gap semiconductor oxide TiO_2 was first studied as a semiconductor electrode for electrochemical photolysis of water into H_2 due to suitable band-edge position, excellent photoelectric properties, high chemical stability, and exceptional photo-corrosion resistance [11,12]. However, there are still many great challenging issues needed to be addressed for TiO_2 photoanode, such as low solar energy utilization efficiency due to its wide band-gap structure and low photon conversion efficiency due to

its high charge carrier recombination rate [13,14]. Thus, a variety of strategies have been developed to solve these issues [15–17]. Particularly, employing narrow band-gap semiconductors to modify TiO_2 for constructing heterojunction structure with type-II band structure has been expected as an efficient method to substantially boost PEC performance, because this heterostructure can improve the solar energy utilization efficiency as well as enhance the separation efficiency of the photoexcited charge carriers [18]. Therefore, several narrow band-gap semiconductors, including $BiVO_4$, In_2S_3, Cu_2O, and CdS [19–22], have been used to modify TiO_2 to fabricate type-II band structure photoanode for enhancing light harvesting and PEC performance.

Among these semiconductors, CdS with a band gap of ca. 2.4 eV is regard as a promising material for modifying TiO_2 because the band matching between TiO_2 and CdS can establish type-II band structure favorable for the charge separation. In addition, CdS can significantly improve visible light harvesting of TiO_2/CdS heterostructure because of narrow band gap of CdS. On the other hand, previous studies have shown that the morphology of CdS nanostructures can greatly affect the PEC or photocatalytic performance of heterojunction photoelectrodes

* Corresponding authors.
  E-mail addresses: sunnyjuan920@163.com (L. Wang), zhouqing2021@muc.edu.cn (Q. Zhou).
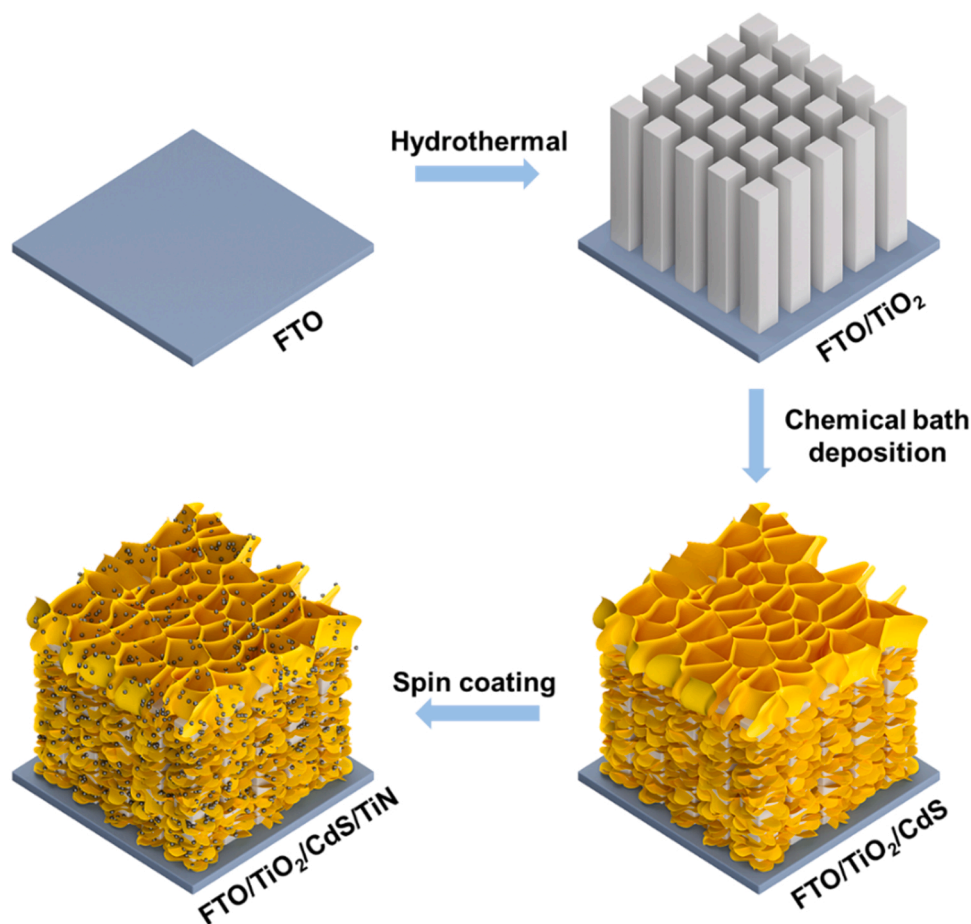
Fig. 1. Schematic fabrication procedure of the ternary TiO$_2$/CdS/TiN NRAs.

[23,24] or photocatalysts [25,26]. In particular, two-dimensional (2D) CdS nanostructures provide large numbers of active sites because of their large specific surface area, enabling the photoexcited charge carriers to be effectively transferred and separated [24]. Considering unique property of 2D CdS nanostructure, modification of 1D TiO$_2$ nanostructure with 2D CdS nanostructure is highly expected to fabricate a 1D/2D TiO$_2$/CdS photoanode that can achieve significantly enhanced visible light absorption and high photogenerated carrier separation efficiency. However, CdS cannot make full use of visible light to split water during PEC reaction because it usually absorbs photon energy above 2.4 eV (less than 520 nm). To solve this issue, some semiconductors with smaller band gaps are used to modify CdS to improve visible light harvesting. For example, CdS/Cu$_2$O and CdS/ZnFe$_2$O$_4$ heterojunctions exhibited the improved visible light absorption, leading to significantly enhanced PEC performance [27,28].

Aside from the above methods, using plasmonic nanoparticles (NPs) to modify CdS is another effective method for improving its visible light absorption and PEC water splitting. As demonstrated in the recent studies, surface plasmon resonance (SPR)-induced visible light harvesting ability of plasmonic NPs enhances the solar-energy utilization. Furthermore, highly energetic hot electrons generated by SPR effect can substantially boost PEC performance because they can inject into the semiconductor conduction band (CB) to take part in water splitting. Notably, the Schottky barrier formed at the metal and semiconductor interface prevents the injected hot electrons from returning to the plasmonic nanostructure [29]. Thus, in this heterostructure, plasmonic metal NPs serve as light absorber and electron provider [30,31]. In the developed plasmonic heterostructures, Au and Ag NPs are extensively used to modify semiconductors to substantially boost PEC performance. It has reported that TiO$_2$/ZnO/Au and CuWO$_4$/Ag photoelectrodes

presented significantly enhanced PEC water splitting achieved by a dual role of plasmonic Au and Ag nanostructure acting as both light absorber and electron provider [32,33]. However, the scarcity and high-cost of noble metals restricts the potential applications of the conventionally plasmonic photoelectrodes. Most recently, titanium nitride (TiN), as one of nonmetal conductive ceramics, has been regarded as a promising plasmonic sensitizer because of its good plasmonic property from visible to near-infrared light [34]. In addition, TiN NPs own merits such as low cost, high thermal and oxidative stability [35]. Based on these unique merits, TiN NPs have been applied to modify semiconductor nanostructure to construct heterostructure photoanode for PEC and photocatalytic water splitting H$_2$ evolution. For example, under zero-bias visible light irradiation, TiN NPs decorated CdS nanorod arrays (NRAs) generated a photocurrent of 2.9 mA cm^{-2} and a H$_2$ generation rate of 101.5 μmol cm^{-2} h^{-1}, which were 1.6-fold and 2.0-fold that of CdS NRAs, respectively. This study revealed that the significantly boosted PEC performance of CdS/TiN NRAs was attributed to the SPR-induced hot electron injection of TiN NPs [36]. Unfortunately, to our best knowledge, there are no any investigations on the PEC H$_2$ evolution of TiN nanoparticle-sensitized TiO$_2$/CdS nanorod array (NRA) photoanode under simulated sunlight irradiation.
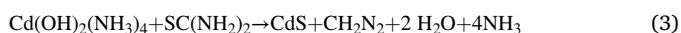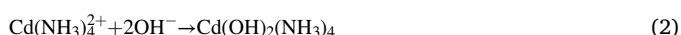
Here, to solve above-mentioned two key problems of low photon energy utilization and high charge carrier recombination rate of TiO$_2$, a TiO$_2$ NRA photoanode integrating type-II band structure and nonmetal plasmonic sensitizer was constructed by successively modifying with 2D CdS nanosheets and TiN NPs (Fig. 1). In this novel ternary photoanode, type-II band structure and nonmetal plasmonic sensitizer are skillfully integrated together. In addition, 2D CdS nanosheets with large surface area not only greatly improve visible light absorption, but also enlarge the contact area with TiO$_2$ to form type-II band structure favorable for

the charge transfer and separation. Furthermore, 2D CdS nanosheets can provide more sites to absorb TiN NPs to further boost photon energy utilization through SPR-induced hot electron injection. The fabricated TiO_2/CdS/TiN NRA photoanode exhibits greatly enhanced PEC H_2 evolution compared to the unmodified TiO_2 NRA photoanode. The tests including electrochemical impedance spectroscopy (EIS), Mott-Schottky (M-S) and photoluminescence (PL) verify that the remarkably improved PEC performance of the ternary photoanode is contributed to SPR-induced hot electron injection of TiN NPs and the efficient charge separation. The present work provides a new perspective for integrating type-II band structure and nonmetal plasmonic sensitizer into a single photoelectrode for efficient solar-driven PEC H_2 evolution.

2. Experimental

2.1. Preparation of TiO_2/CdS NRAs

TiO$_2$ NRAs were prepared on clean fluorine-doped tin oxide (FTO) glasses by a similar hydrothermal method as reported in previous work [21]. Firstly, 14 mL of concentrated hydrochloric acid and 16 mL of deionized water were mixed and stirred for 10 min, followed by slowly dropping 560 μL of titanium butoxide into the aqueous solution under vigorous stirring to get a transparent solution. Secondly, the solution was poured into Teflon-lined stainless autoclave and two pieces of cleaned FTO substrate with conductive side downward were immersed into the solution, followed by heating at 150 ℃ for 3.5 h. After naturally cooling, the prepared samples were washed with deionized water and dried in air, and then annealed at 450 ℃ for 30 min in a tubular furnace. Then 2D CdS nanosheets were grown on TiO$_2$ NRAs through a facile chemical bath deposition (CBD) method. In a typical process, 0.12 M CdCl$_2$·2.5 H$_2$O, 1.2 M NH$_4$Cl, 1.2 M KOH and 0.06 M CH$_4$N$_2$S solution were poured into an alkali resistant container successively, followed by immersing TiO$_2$ NRAs grown on the FTO and reacting in the water bath for 15 min at 90 ℃. Finally, the samples were washed with deionized water and then dried at 60 ℃ for 2 h. The main chemical reactions for the formation of CdS are given as follows [37]:

$$Cd^{2+}+4NH_3 \rightarrow Cd(NH_3)_4^{2+} \tag{1}$$

$$Cd(NH_3)_4^{2+}+2OH^- \rightarrow Cd(OH)_2(NH_3)_4 \tag{2}$$

$$Cd(OH)_2(NH_3)_4+SC(NH_2)_2 \rightarrow CdS+CH_2N_2+2 H_2O+4NH_3 \tag{3}$$

For the sake of comparison, 2D CdS nanosheets were directly prepared on FTO glasses using the same method described above according to the following parameters: the cleaned FTO glasses were immersed into the reaction solution and followed by reacting in the water bath for 30 min at 90 ℃.

2.2. Fabrication of TiO_2/CdS/TiN NRAs

TiN NPs were deposited on TiO$_2$/CdS NRAs using a spin-coating method to fabricate TiO$_2$/CdS/TiN NRAs. Firstly, 4 mg of the purchased TiN powders (20 nm) was dispersed in ethyl alcohol (100 mL) and ultrasonic for 30 min. Secondly, 500 μL of the above solution was spin-coated on the as-prepared TiO$_2$/CdS NRAs at 3000 rpm for 30 s. The deposition of TiN NPs was repeated 60 times. For comparison, TiN nanoparticle-modified CdS nanosheets (CdS/TiN) were prepared using a same method to deposite TiN NPs on the 2D CdS nanosheet surface.

2.3. Characterizations

The crystal structure and surface compositions were studied by X-ray diffraction (XRD, Rigaku Ultima IV) and X-ray photoelectron spectroscopy (XPS, Thermo Scientific K-Alpha), respectively. The morphology and microstructure features of the obtained samples were observed by scanning electron microscopy (SEM, HITACHI S-4800) and transmission
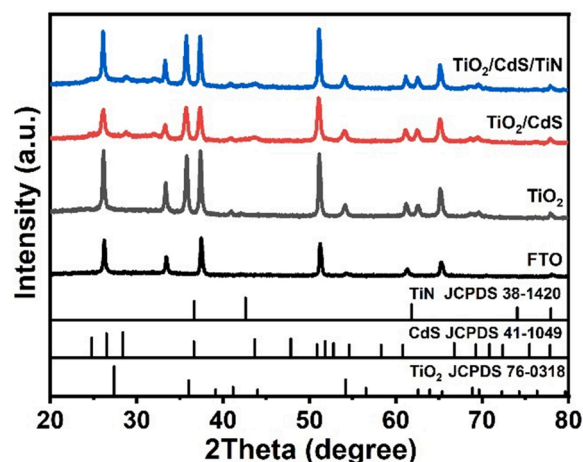
Fig. 2. XRD patterns of the TiO$_2$, TiO$_2$/CdS and TiO$_2$/CdS/TiN NRAs.

electron microscopy (TEM, JEOL JEM-2800). A Lambda 950 UV/Vis/NIR spectrophotometer (PerkinElmer) was applied to evaluate the light harvesting property. A Horiba laser Raman spectrometer (LabRAM HR Evolution) with an excitation wavelength of 532 nm was used to collect Raman spectra. A FLS920 fluorescence spectrometer (Edinburgh) was employed to evaluate the room-temperature PL property under 325 nm light excitation.

2.4. PEC and H_2 production measurements

The PEC performance of the as-prepared photoanodes was measured in a three-electrode electrochemical workstation (CHI 760E) under a 300 W Xenon lamp with an AM 1.5 G filter. Three electrodes are the working electrode (samples), reference electrode (Ag/AgCl) and counter electrode (Pt wire), respectively. The electrolyte was a mixed solution of 0.25 M Na$_2$SO$_3$ and 0.35 M Na$_2$S aerated with nitrogen for 20 min at a pH of about 13. The working electrodes were irradiated with simulated sunlight during the PEC tests at a light power density of 100 mW cm^{-2}. An incident photon-to-current conversion efficiency (IPCE) testing system (Newport QE/IPCE) was used to measure IPCE under a series of monochromatic light without applying bias vs. Ag/AgCl. EIS property was studied in the frequency range of 0.1–10^5 Hz under open circuit potential. The volumes of H$_2$ generated by the photoanodes during PEC reaction was measured by an improved displacement method. The cyclic voltammetry (CV) measurements were conducted in the non-Faradaic region at several scan rates of 20, 40, 60, 80, 100 and 120 mV s^{-1}. The potential window was 0.08 V and the initial scanning point was located around the open circuit potential.

3. Results and discussion

3.1. Characterization

The composition and crystalline structure of the TiO$_2$, TiO$_2$/CdS and TiO$_2$/CdS/TiN NRAs were determined by XRD. Fig. 2 demonstrate that the unmodified TiO$_2$ exhibits rutile phase structure and the all peaks match well with (112), (301), (002), (211), (111) and (101) crystalline planes (JCPDS No.76–0318). For TiO$_2$/CdS NRAs, the peaks at 28.5° and 44.0° were respectively indexed to (101) and (110) planes of Hexagonal phase CdS (JCPDS No. 41–1049). XRD plot of TiO$_2$/CdS/TiN NRAs does not display obvious peaks of TiN NPs, suggesting a low TiN loading in the sample. Raman spectroscopy was applied to provide more insights into the structural information of the TiO$_2$/CdS/TiN heterostructure (Fig. S1). For the pure TiO$_2$ NRAs, three Raman peaks located at 232 cm^{-1}, 445 cm^{-1} and 609 cm^{-1} can be assigned to the B1g, Eg and A1g vibrational modes of TiO$_2$. [38] In comparison to TiO$_2$ NRAs, two
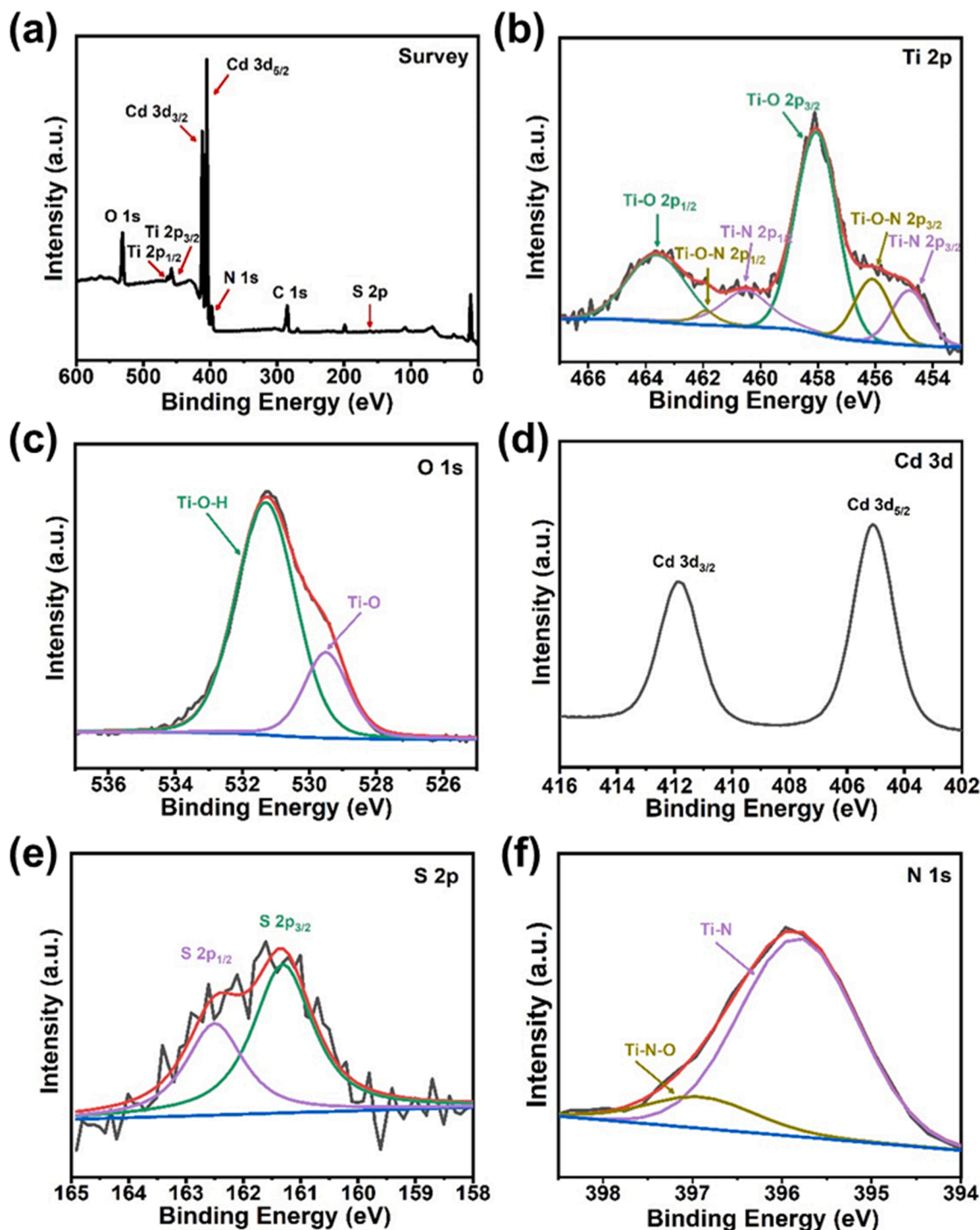
Fig. 3. (a) The survey XPS spectra of the TiO₂/CdS/TiN NRAs. High-resolution XPS spectra of the TiO₂/CdS/TiN NRAs: (b) Ti 2p, (c) O 1s, (d) Cd 3d, (e) S 2p and (f) N 1s.

additional small characteristic peaks at 328 cm^{-1} and 536 cm^{-1} can be observed in the TiO₂/CdS/TiN NRAs, which can be assigned to the longitudinal acoustic (LA) mode and transverse optical (TO) mode of the TiN NPs. [39] Therefore, the Raman results indicate the existence of TiN in TiO₂/CdS/TiN heterostructure.

XPS spectra were applied to further study the composition and elemental valence state of the as-prepared sample. As shown in Fig. 3a, the typical survey spectrum obviously confirms the presence of Ti, O, Cd, S and N elements in the samples. The high resolution XPS spectra of

these five elements were measured to analyze their elemental valence states. In Fig. 3b, the high resolution XPS spectrum of Ti 2p can be split into six peaks. Two peaks at 458.1 and 463.6 eV can be ascribed to Ti $2p_{3/2}$ and $2p_{1/2}$ of Ti in the TiO₂ crystal [40], peaks at 456.1 and 461.9 eV are assigned to Ti $2p_{3/2}$ and $2p_{1/2}$ in the Ti-O-N [41], and peaks at 454.8 and 460.5 eV are indexed to Ti $2p_{3/2}$ and $2p_{1/2}$ of Ti in TiN [41]. O 1 s XPS spectrum in Fig. 3c can be divided into two peaks. The peak with binding energy at 529.5 eV can be ascribed to Ti-O of TiO₂, while the peak (531.3 eV) may come from the adsorbed H₂O on the surface
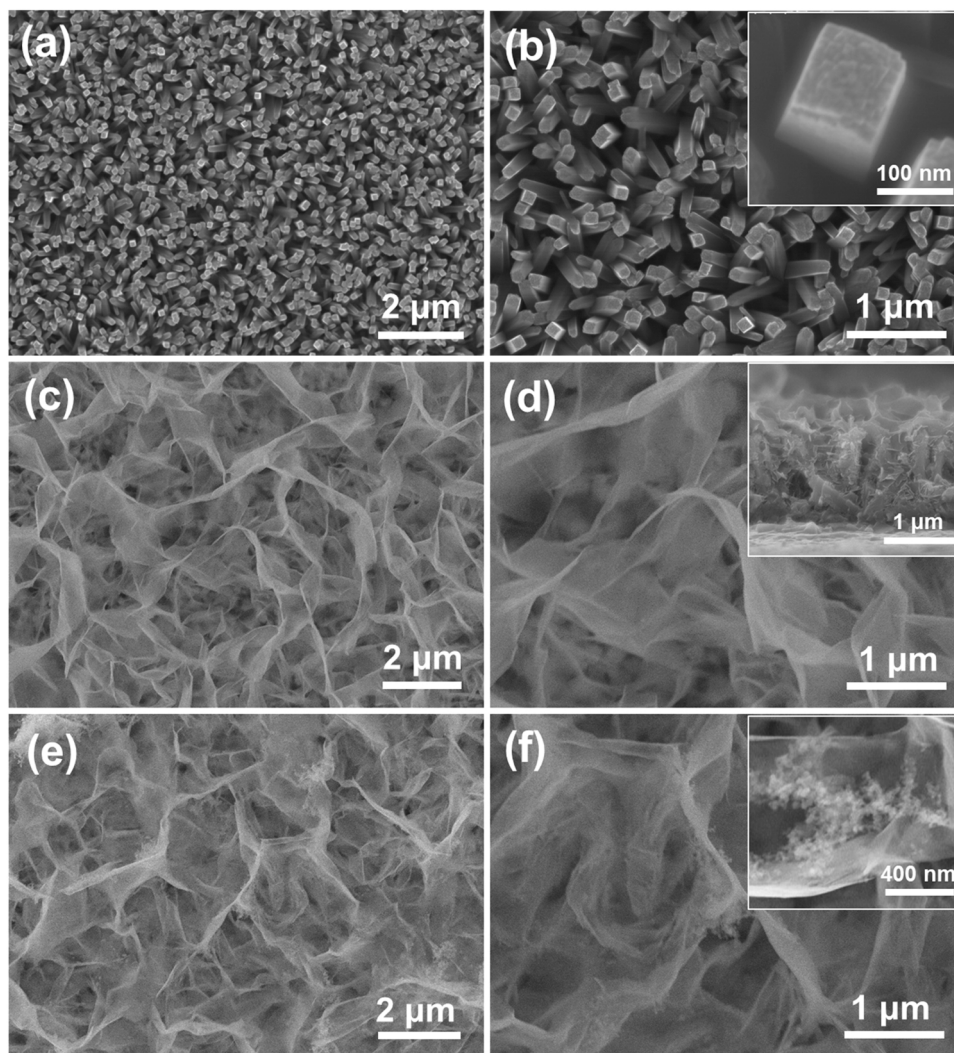
Fig. 4. Typical SEM images of (a, b) TiO_2 NRAs, (c, d) TiO_2/CdS NRAs and (e, f) $TiO_2/CdS/TiN$ NRAs.

(Ti-O-H) of the samples [42]. In Fig. 3d, the peaks located at 405.1 and 411.9 eV originate from Cd $3d_{5/2}$ and $3d_{3/2}$ of Cd^{2+} in CdS. In S 2p XPS spectrum, two peaks at binding energies of 161.3 and 162.5 eV are assigned to S $2p_{3/2}$ and $2p_{1/2}$ (Fig. 3e). As demonstrated in previous work, these two binding modes are attributed to S^{2-} in CdS [27]. In Fig. 3f, the peak at 395.8 eV is indexed to Ti-N and the peak at 396.9 eV is assigned to Ti-O-N of TiN [40]. Thus the XPS measurements and corresponding analyses evidently confirm that the exist of TiN in the heterogeneous nanoarrays, demonstrating successful construction of $TiO_2/CdS/TiN$ NRAs. Meanwhile, the variety of element binding energy can directly reflect the changes of electron density. The increase of binding energy represents the decrease of the electron density, while the decrease of binding energy demonstrates the increase of the electron density. Therefore, the binding energy change can be used to examine the direction of charge carrier transfer in the heterojunction photo-electrode [43]. As displayed in Fig. S2a and b, the binding energies of Ti 2p in TiO_2/CdS heterojunction structure obviously shift toward lower energy levels, compared with that of pure TiO_2, indicating an increase in the electron density of TiO_2 in TiO_2/CdS heterojunction. In contrast, compared with that of pure CdS, the binding energies of Cd 3d in TiO_2/CdS heterojunction structure significantly shift to higher energy levels, implying that the electrons migrate from CdS to TiO_2. Additionally, in comparison with that of pure TiN, the binding energies of Ti 2p in CdS/TiN heterojunction structure obviously shift toward lower energy levels, indicating an increase in the electron density of TiN in CdS/TiN

heterojunction. While compared with that of pure CdS, the binding energies of Cd 3d in CdS/TiN heterojunction structure significantly shift to higher energy levels, implying that the electrons migrate from CdS to TiN.

Fig. 4 shows the SEM photographs of the as-obtained TiO_2 NRAs. The low-magnification SEM photograph of Fig. 4a demonstrates that the vertically aligned TiO_2 rod-like nanostructures are grown on the whole surface of FTO substrate. The high-magnification SEM photograph of Fig. 4b clearly shows that these ordered TiO_2 NRAs present the morphology of regular quadrangular prism. The enlarged SEM image of a TiO_2 nanorod (inset of Fig. 4b) shows that the cross-section diameter of the TiO_2 NRA is around 130 nm. Fig. 4c and d presents SEM photographs of TiO_2/CdS NRAs taken from low and high magnifications. After modifying with 2D CdS nanosheets, the top of TiO_2 NRAs was completely covered by the ultrathin CdS nanosheets with a smooth surface. Additionally, the cross-sectional view SEM image of TiO_2/CdS NRAs (inset of Fig. 4d) shows that these ultrathin CdS nanosheets insert into the spaces between the TiO_2 NRAs and entirely sheathe on the whole surface of TiO_2 NRA. Fig. 4e and f exhibits the SEM images of $TiO_2/CdS/TiN$ NRAs at low and high magnifications, respectively. SEM images apparently show that the surface of CdS nanosheets is coated with many TiN NPs with small size and becomes rough. As clearly demonstrated in the enlarged SEM image of inset in Fig. 4f, a large number of TiN NPs with small size are attached to the surface of CdS nanosheets and some of TiN NPs tend to agglomerate together due to
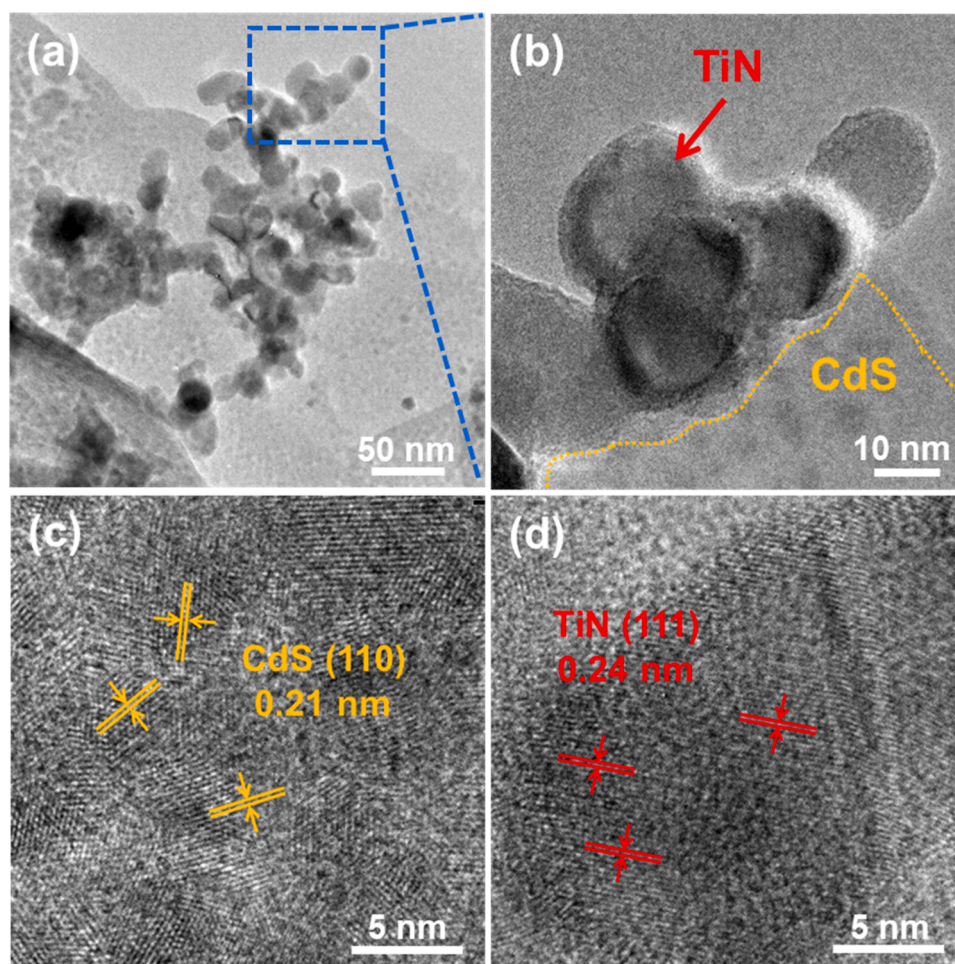
Fig. 5. (a) TEM image and (b-d) HRTEM images of the TiO$_2$/CdS/TiN NRAs.

their small particle size. For a comparison, 2D CdS nanosheets and CdS/TiN were directly prepared on the FTO substrate (Fig. S3).

The microstructure feature of TiO$_2$/CdS/TiN NRAs was further investigated by TEM and high-resolution TEM (HRTEM). TEM image apparently shows that some TiN NPs are attached to the surface of the CdS nanosheet, as demonstrated in Fig. 5a. In the HRTEM image of Fig. 5b, the tight connections of TiN NPs and CdS nanosheet can be clearly seen, which are conducive to the interface charge migration. Fig. 5c and d shows the high-magnification HRTEM images of the typical CdS nanosheet and TiN nanoparticle, respectively. As shown in Fig. 5c, the lattice fringes with a spacing of 0.21 nm correspond to (110) crystal planes of CdS. In Fig. 5d, the HRTEM image exhibits lattice fringes with a spacing of 0.24 nm, corresponding to (111) crystal planes of TiN. Above experimental results and analyses confirm that the TiO$_2$/CdS/TiN NRAs have been successfully fabricated via successively modifying with 2D CdS nanosheets and TiN NPs.

The light absorption spectra were collected from 300 to 800 nm, as exhibited in Fig. 6a. Apparently, the pure TiO$_2$ NRAs only exhibits remarkable absorption less than 400 nm with the strongest light absorption peak located at around 360 nm, which is contributed by the characteristic light absorption of rutile TiO$_2$ crystal [44]. In contrast with the TiO$_2$ NRAs, the TiO$_2$/CdS NRAs present obvious visible light absorption in the wavelength range from 400 to 570 nm. The enhanced light harvesting of the TiO$_2$/CdS NRAs is attributed to the visible light absorption capability of CdS nanosheets [45]. Hence, the light absorption of TiO$_2$/CdS NRAs is significantly extended to the visible light region. Compared to that of the TiO$_2$/CdS NRAs, after decoration with TiN NPs on CdS nanosheets, SPR effect of the TiN NPs dramatically enhances

the visible light absorption of as-constructed TiO$_2$/CdS/TiN NRAs in the region from 570 to 800 nm. The light absorption property of pure TiN NPs was further measured to confirm the SPR effect, as displayed in Fig. S4. The absorption spectrum of TiN NPs exhibits a broad SPR peak over the range of 500–1400 nm with an obvious absorption peak at about 690 nm. The absorption behavior of the TiN NPs is consistent with the previous studies [46,47]. This wider SPR absorption feature for the TiN NPs can be ascribed to intrinsic characteristic of TiN. Additionally, in light absorption spectrum of TiO$_2$/CdS/TiN NRAs, no obvious absorption peak of TiN NPs is seen, possibly resulting from the overlap of the characteristic absorption of 2D CdS nanosheets (ca. 520 nm) and the dominant SPR absorption of TiN NPs (ca. 500 nm). In addition, UV-Vis transmittance and diffuse reflectance spectra of the as-constructed photoanodes were tested and employed to further investigate their optical poetries. As shown in Fig. S5, the TiO$_2$/CdS/TiN NRAs display the lowest reflectance and transmittance in the whole visible region, indicating that the ternary heterogeneous nanoarrays can effectively inhibit surface reflection and enhance light absorption. Thus, it is benefit from the synergistic effect of 2D CdS nanosheets and TiN NPs on the light absorption, the as-constructed TiO$_2$/CdS/TiN NRAs effectively improve utilization of solar energy, thereby expecting to achieve substantially improved PEC performance.

3.2. PEC properties

The PEC activity of the as-prepared samples was tested with a standard three-electrode potentiostat system in a mixed electrolyte of 0.35 M Na$_2$S and 0.25 M Na$_2$SO$_3$ under bias-free simulated sunlight
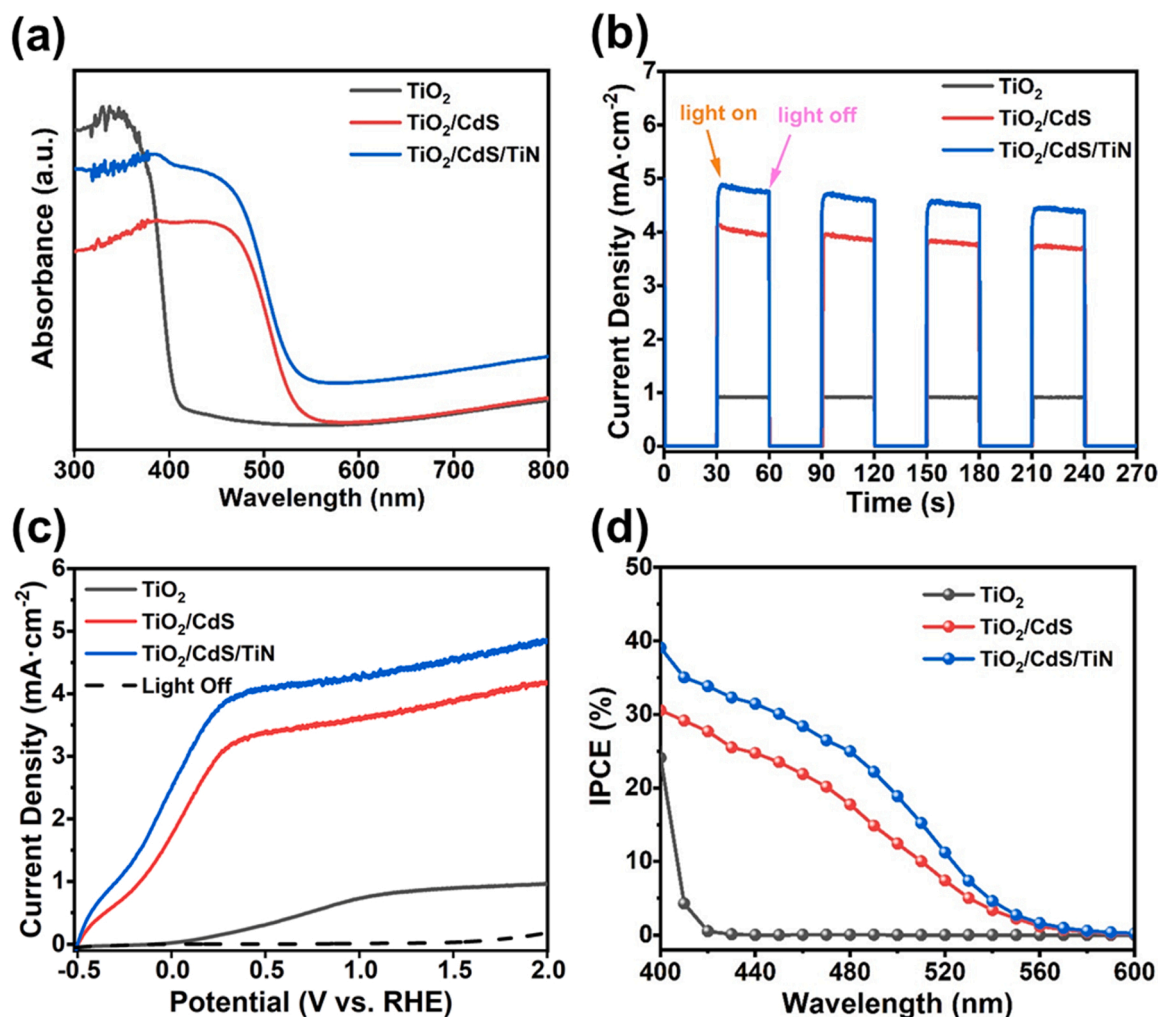
Fig. 6. (a) UV-Vis absorption spectra, (b) Transient photoresponse under bias-free simulated sunlight illumination, (c) LSV curves and (d) IPCE curves of the TiO$_2$, TiO$_2$/CdS and TiO$_2$/CdS/TiN NRAs.

illumination. Fig. 6b shows the transient photoresponse for the as-prepared photoanodes. When as-fabricated photoanodes were illuminated by simulated sunlight, the photocurrent density of each photoanode instantaneously reached up to the maximum value and reverted to the initial stage immediately after the light was turned off, revealing that all the as-fabricated photoanodes possess excellent photoresponse capability during the PEC water splitting process. The photocurrent density generated on the pristine TiO$_2$ NRA photoanode is about 0.92 mA cm^{-2}. After decoration with 2D CdS nanosheets, the TiO$_2$/CdS NRA photoanode generates a drastically enhanced photocurrent density of 4.0 mA cm^{-2}. Furthermore, upon the decoration of the TiN NPs, the photocurrent density of TiO$_2$/CdS/TiN NRA photoanode further increases to 4.5 mA cm^{-2}, 4.9-fold that of TiO$_2$ NRA photoanode. However, when TiO$_2$ NRA photoanode was modified by TiN NPs, the photocurrent density of the TiO$_2$/TiN NRA photoanode is only about 1.2 mA cm^{-2} and the photocurrent onset potential exhibits no obvious cathodic shift, as shown in Fig. S6. Thus, the tests of photocurrent density evidently demonstrate that the drastically enhanced photocurrent density of the TiO$_2$/CdS/TiN NRA photoanode is attributed to the cooperative effects of SPR effect of TiN NPs and type-II heterojunction between TiO$_2$ and CdS interface. Additionally, when the number of repeats for the deposition of TiN NPs via a spin-coating method is further increased to 90 times, the as-prepared TiO$_2$/CdS/TiN NRA photoanode shows a decrease in photocurrent density, as demonstrated in I-t and LSV curves (Fig. S7). As shown in Fig. S8, it is clearly seen that the TiN spin-

coating repeats show an obvious effect on the coverage of TiN NPs on the surface of CdS nanosheet. When the number of repeats for the loading of TiN NPs increases to 90 times, the excess TiN NPs accumulates together with each other to form aggregates with larger size on the surface of CdS nanosheets. These aggregates are unfavorable for charge transfer and separation on interface of CdS and TiN, leading to the decreased photocurrent density. Thus, in the following studies, we use the TiO$_2$/CdS/TiN NRA photoanode prepared with 60 spin-coating repeats to investigate the PEC performances.

The above photocurrent tests confirm that SPR effect of TiN NPs plays a key role for the significantly augmented PEC performance of TiO$_2$/CdS/TiN NRA photoanode. In order to compare effect of the SPR effect of TiN NPs on the PEC performance TiO$_2$/CdS NRA photoanode with the Au NPs on identical TiO$_2$/CdS NRA photoanode, the Au NPs with almost same particle size (20–30 nm) as TiN NPs were synthesized and then were used to sensitize TiO$_2$/CdS NRA photoanode for the test of photocurrent density, as shown in Fig. S9a-d. The I-t and LSV curves clearly demonstrate that the TiN NPs exhibit stronger SPR effect to boost PEC performance of TiO$_2$/CdS NRA photoanode than Au NPs with same particle size as the TiN NPs (Fig. S9e and f).

On the other hand, the stability of the photoanode during the PEC reaction is great of importance for its application. To this end, the pH value of the electrolyte during or after the PEC measurement for the TiO$_2$/CdS/TiN NRA photoanode was tested, since the change of pH value of the electrolyte during or after the PEC measurement could

Table 1
The PEC performance of different TiO_2/CdS based ternary heterostructure photoanodes.

Photoanode	Morphology	Photocurrent density (bias)	Light and intensity	Electrolyte	Ref.
TiO_2/CdS/TiO_2	TiO_2 nanorod arrays /CdS nanoparticles	2.1 mA cm^{-2} (0 V vs. Ag/AgCl)	$\lambda \geq 420$ nm 130 mW cm^{-2}	0.1 M Na_2S	[48]
TiO_2/CdS/CdSe	TiO_2 nanorod arrays /CdS nanoparticles	2.01 mA cm^{-2} (0.2 V vs. Ag/AgCl)	AM 1.5 G 100 mW cm^{-2}	0.01 M Na_2S+ 0.01 M Na_2SO_3	[49]
TiO_2/CdS/MoS_2	TiO_2 nanorod arrays /CdS nanocrystals	3.25 mA cm^{-2} (0.5 V vs. RHE)	AM 1.5 G 100 mW cm^{-2}	0.25 M Na_2S+ 0.35 M Na_2SO_3	[50]
TiO_2/CdS/Co-Pi	TiO_2 nanowire arrays /CdS nanoparticles	0.8 mA cm^{-2} (0 V vs. Ag/AgCl)	AM 1.5 G 100 mW cm^{-2}	0.1 M sodium phosphate	[20]
TiO_2/CdS/Bi_2S_3	TiO_2 nanotube arrays /CdS quantum dots	2.16 mA cm^{-2} (0.74 V vs. Ag/AgCl)	AM 1.5 G 100 mW cm^{-2}	0.25 M Na_2S+ 0.35 M Na_2SO_3	[51]
TiO_2/CdS/PbS	TiO_2 nanotube arrays /CdS quantum dots	4.1 mA cm^{-2} (0.1 V vs. Ag/AgCl)	AM 1.5 G 100 mW cm^{-2}	0.25 M Na_2S+ 0.35 M Na_2SO_3	[52]
TiO_2/CdS/TiN	TiO_2 nanorod arrays /CdS nanosheets	4.5 mA cm^{-2} (0 V vs. Ag/AgCl)	AM 1.5 G 100 mW cm^{-2}	0.35 M Na_2S+ 0.25 M Na_2SO_3	This work

reflect the stability of the photoanode. The result shows that pH values are 13.3 and 13.4 before and after measurement, respectively, demonstrating no obvious change in pH value of the electrolyte before and after the PEC measurements of the TiO_2/CdS/TiN NRA photoanode. Moreover, the stability of TiO_2/CdS/TiN NRA photoanode was further evaluated by testing photocurrent density in electrolyte with different pH, which was prepared by controlling the concentration of Na_2S. The results clearly demonstrate that the as-fabricated TiO_2/CdS/TiN photoanode shows stable photoresponse capability and similar photocurrent onset potential in the four kinds of electrolytes with different pH values

and possesses the highest photocurrent density in the 0.25 M Na_2SO_3 and 0.35 M Na_2S electrolyte, as presented in Fig. S10. Thus, in the following studies, the PEC performances of the photoanodes were tested in 0.25 M Na_2SO_3 and 0.35 M Na_2S electrolyte.

The improved PEC property of the as-fabricated photoanodes was further confirmed by linear sweep voltammetry (LSV) measurements at an applied bias of −1.5–1.0 V vs. Ag/AgCl, as shown in Fig. 6c. In each LSV curve of the sample, the photocurrent density augments with the applied bias for all photoanodes under simulated sunlight irradiation. However, the TiO_2/CdS/TiN NRA photoanode not only shows the
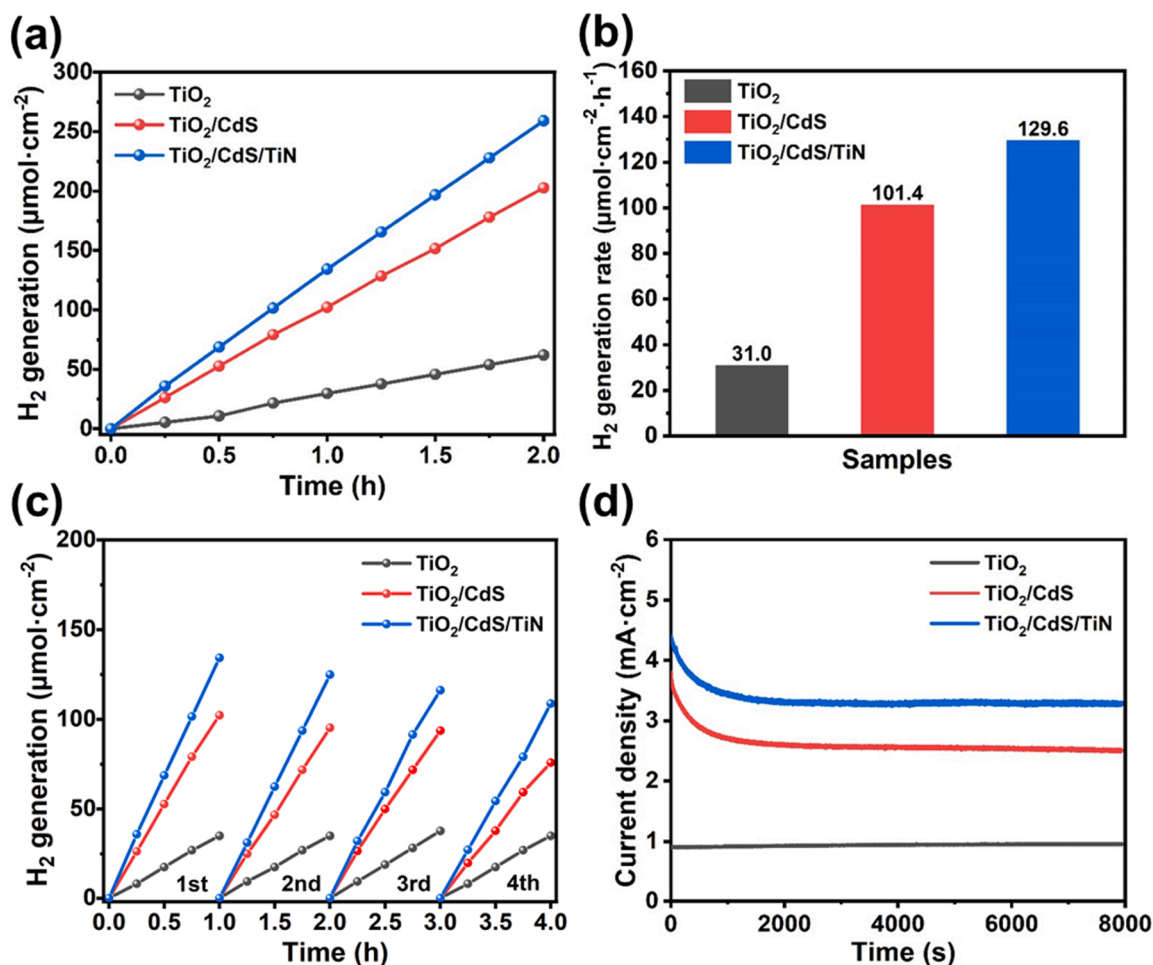
Fig. 7. (a) Time-dependent H_2 yields, (b) average H_2 generation rate, (c) cycling experiments and (d) long-term PEC stability of the TiO_2, TiO_2/CdS and TiO_2/CdS/TiN NRA photoanodes under bias-free simulated sunlight irradiation.

significant augment in the photocurrent with the applied bias, but also exhibits an obvious cathodic shift of photocurrent onset potential, indicating a remarkable improvement in the surface charge transfer efficiency after the decoration of CdS and TiN, and hence bringing about water oxidation at the low potential range. The substantially improved PEC performance indicates that the 2D CdS nanosheets with high photon-harvesting ability and plasmonic TiN NPs indeed contributed to the improved PEC performance. Table 1 presents a detailed comparison of the PEC performance of the as-fabricated TiO$_2$/CdS/TiN photoanode with other relative TiO$_2$/CdS based ternary heterostructure photoanodes [20,48–52]. As shown in Table 1, there are very limited studies on the PEC performances of the ternary TiO$_2$/CdS based heterostructure photoanodes. Moreover, in contrast with other relative TiO$_2$/CdS based ternary heterostructure photoanodes, the as-fabricated TiO$_2$/CdS/TiN photoanode achieves the highest photocurrent density, exhibiting the significantly enhanced PEC water splitting capability and potential applications in PEC water splitting for H$_2$ generation. As well known, the good interfacial contact between the photoanode surface and electrolyte is a prerequisite for achieving an effective PEC reaction. As shown in Fig. S11, the static contact angles of water dripped on the TiO$_2$, TiO$_2$/CdS and TiO$_2$/CdS/TiN NRAs are 13.47°, 19.73° and 23.49°, respectively. Although the TiO$_2$/CdS and TiO$_2$/CdS/TiN NRAs show larger water contact angle compared with pure TiO$_2$ NRAs, their water contact angles are still much lower than 90°, indicating that they are hydrophilic. This excellent hydrophilic behavior is beneficial not only for the contact between the photoanode and electrolyte, but also for diffusion of ions.

To quantify the wavelength-dependent photon conversion efficiency, we carried out the measurements for IPCE of the photoanodes in the wavelength range of 400–600 nm. The IPCE values were estimated by the following equation [53]:

$$IPCE = \frac{1240(V \times nm) \times |J_{ph}(mA \cdot cm^{-2})|}{P_{mono}(mW \cdot cm^{-2}) \times \lambda(nm)} \qquad (4)$$

where J_{ph}, P_{mono} and λ are the photocurrent density at a specific wavelength, the monochromatic incident light power density and the incident light wavelength, respectively. As shown in Fig. 6d, IPCE results demonstrate that the decorations with CdS nanosheets and TiN NPs significantly extend the light response range and boost the photoelectric conversion efficiency of the TiO$_2$ photoanode. Apparently, the IPCE curves of TiO$_2$/CdS and TiO$_2$/CdS/TiN NRA photoanodes demonstrate a broadened photoresponse in the range from 400 to 580 nm and the IPCE values are significantly improved by comparison with the pristine TiO$_2$

NRA photoanode. More importantly, within the entire test wavelength range, the TiO$_2$/CdS/TiN NRA photoanode shows a substantial enhancement for IPCE, which is in good coincidence with the above absorption spectra as presented in Fig. 6a. The TiO$_2$/CdS/TiN NRA photoanode achieves the maximum IPCE value of 39.1% at the wavelength of 400 nm. The IPCE measurements verify that the photogenerated charge carriers can be efficiently separated and transferred in the TiO$_2$/CdS/TiN NRA photoanode, substantially boosting PEC performance.

Based on the LSV test results, values of the solar-to-hydrogen (STH) conversion efficiency (η) that can be used to further evaluate capability of the photoanodes for PEC H$_2$ generation were calculated using the following equation [54,55]:

$$\eta = \frac{J_{ph}(mA/cm^2) \times E^0(V) \times \eta_F}{P_{total}(mW/cm^2)} \times 100\% \qquad (5)$$

From this equation, the STH conversion efficiency can be determined by the photocurrent density (J_{ph}) at zero bias, the thermodynamic reaction potential ($E^0 = 0.21$ V) for oxidation of sacrificial agents Na$_2$SO$_3$ and Na$_2$S during the PEC water splitting reaction [48], the Faradaic efficiency (η_F) of hydrogen production at the standard conditions and the total incident solar irradiation power density (P_{total}). The calculated STH values are 0.15%, 0.76% and 0.89% for TiO$_2$, TiO$_2$/CdS and TiO$_2$/CdS/TiN NRA photoanodes, respectively, showing that the STH conversion efficiency of TiO$_2$/CdS/TiN NRA photoanode is the highest among the all photoanodes, which is approximately 6 times higher than that of pristine TiO$_2$ NRA photoanode.

3.3. PEC hydrogen evolution

The bias-free simulated light-driven PEC hydrogen evolution of the obtained photoanodes was evaluated in a mixture electrolyte solution of Na$_2$S and Na$_2$SO$_3$. Fig. 7a demonstrates the H$_2$ yields generated by the photoanodes under simulated light illumination for 2 h. It is clearly shown that the H$_2$ yields augment linearly with irradiation time of light, indicating a stable PEC H$_2$ generation ability and good photostability of the prepared photoanodes. Furthermore, the TiO$_2$/CdS/TiN NRA photoanode exhibits dramatically enhanced capacity for PEC H$_2$ generation and achieves a H$_2$ yield of 259.2 μmol cm^{-2} during the 2 h light irradiation. Fig. 7b exhibits histograms of average H$_2$ generation rates for the as-prepared photoanodes. The H$_2$ generation rates of TiO$_2$ and TiO$_2$/CdS NRA photoanodes are separately 31.0 and 101.4 μmol cm^{-2} h^{-1}. Nevertheless, the TiO$_2$/CdS/TiN NRA photoanode acquires a H$_2$
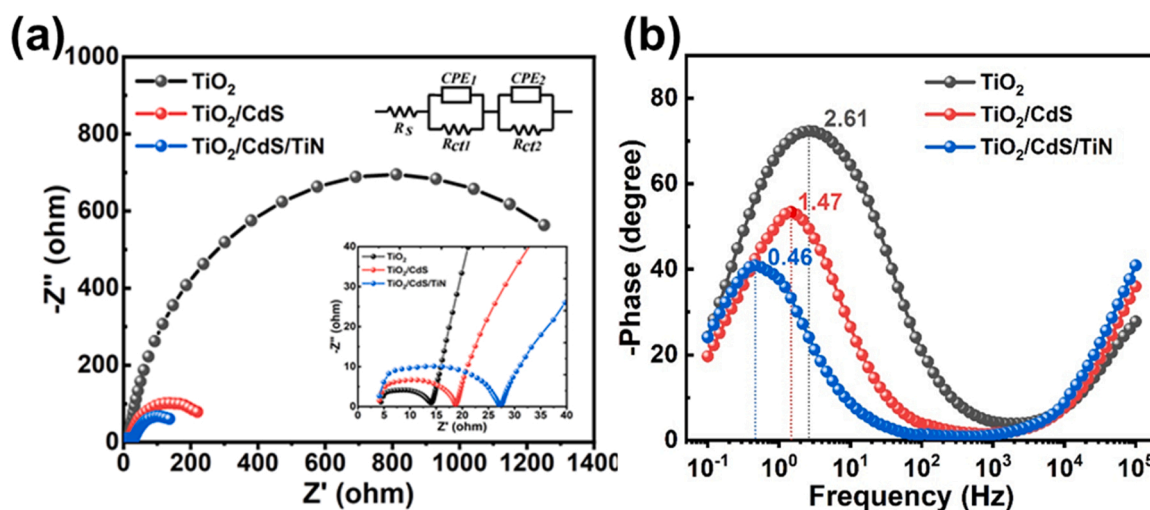

Fig. 8. EIS spectra of the TiO$_2$, TiO$_2$/CdS and TiO$_2$/CdS/TiN NRAs: (a) Nyquist plots and (b) Bode phase plots. Top-right inset in (a): the equivalent circuit model for Nyquist plots. Bottom-right inset in (a): the amplifying Nyquist plots in the high-frequency region.

Table 2
The fitting parameters of the equivalent circuit for the TiO_2, TiO_2/CdS and $TiO_2/CdS/TiN$ NRAs.

Samples	R_s (Ω cm^2)	R_{ct1} (Ω cm^2)	CPE_1 (s^n/Ω cm^2)	n_{dl1}	R_{ct2} (Ω cm^2)	CPE_2 (s^n/Ω cm^2)	n_{dl2}
TiO_2	3.685	1606	4.712×10^{-4}	0.9130	1.046	1.091×10^{-6}	0.8765
TiO_2/CdS	3.622	243	2.147×10^{-3}	0.8902	1.500	2.578×10^{-7}	0.9600
$TiO_2/CdS/TiN$	2.421	174	5.514×10^{-3}	0.8364	2.470	3.591×10^{-7}	0.8977

production rate of 129.6 µmol cm^{-2} h^{-1}, which is approximately 4.2-fold and 1.3-fold that of TiO_2 and TiO_2/CdS NRA photoanode, respectively. In addition, the Faradaic efficiencies of the as-prepared photoanodes were also determined by comparing consumed electrons with the amount of generated H$_2$ [56,57]. The calculated Faradaic efficiencies for TiO_2, TiO_2/CdS and $TiO_2/CdS/TiN$ NRA photoanodes during PEC H$_2$ generation test for 2 h under light irradiation are 88.77%, 93.13% and 98.20%, respectively (Fig. S12).

The cycling experiments for H$_2$ generation of the photoanode were also measured under light irradiation. As shown in Fig. 7c, the yields of H$_2$ generated from the $TiO_2/CdS/TiN$ NRA photoanode decrease slightly after four cycles without renewing the electrolyte and the photoanode, confirming that the $TiO_2/CdS/TiN$ NRA photoanode shows a good stability. Long-term PEC stability of photoanodes is another key factor for practical applications of PEC cells. The photocurrent stabilities of the different photoanodes were examined during H$_2$ generation experiments under simulated light illumination for 8000 s. As presented in Fig. 7d, the photocurrent densities of TiO_2/CdS and $TiO_2/CdS/TiN$ NRA photoanodes decrease slightly at the initial stage, and then tend to stable. More importantly, the photocurrent density of $TiO_2/CdS/TiN$ NRA photoanode retains at 3.3 mA cm^{-2} after long-term light irradiation for 8000 s without applying any bias. Additionally, the SEM images of the $TiO_2/CdS/TiN$ NRA photoanode exhibits no obvious morphological and structural change after long-term PEC measurements (Fig. S13a, b). The energy dispersive spectroscopy (EDS) elemental mappings of the $TiO_2/CdS/TiN$ NRA photoanode demonstrate that the Ti, O, Cd, S, N elements uniformly disperse in the ternary heterogeneous nanoarrays, as exhibited in Fig. S14a-g. The results show that the CdS nanosheets and TiN NPs are still adhered well to the TiO_2 NRAs after long-term PEC measurements, further confirming the good stability of the as-prepared $TiO_2/CdS/TiN$ NRA photoanode. The above results experimentally confirm the crucial role of CdS nanosheets and TiN NPs in improving the PEC H$_2$ production capability for the $TiO_2/CdS/TiN$ NRA photoanode.

3.4. Mechanism

To better understand the enhanced PEC performance of the $TiO_2/CdS/TiN$ NRA photoanode, the separation and transfer behavior of photogenerated charge carriers in all photoanodes were assessed using the EIS measurements. Fig. 8a shows the typical Nyquist plots of the photoanodes at a frequency range of 0.1–10^5 Hz under simulated sunlight irradiation. As seen in Fig. 8a, all the Nyquist plots present a large semicircle in the low-frequency range and a small semicircle in the high-frequency range, which correspond to the charge transfer resistances at the photoanode-electrolyte interface and the counter electrode-electrolyte interface, respectively. Among all photoanodes, the $TiO_2/CdS/TiN$ NRA photoanode processes the smallest semicircle arc diameter. The results reflect that the charge transfer resistance in $TiO_2/CdS/TiN$ NRA photoanode can be obviously reduced, resulting in the fastest separation and transfer of photogenerated charge carriers. For further quantitative analysis, the equivalent circuit model for interpreting the experimental EIS data has been constructed and illustrated in Fig. 8a. Table 1 gives the relative fitting parameters. Charge transfer resistances at low and high frequency are referenced as R_{ct1} and R_{ct2}, and constant phase elements at low and high frequency are referenced as CPE_1 and CPE_2, respectively. R_s defines as the series resistance in the PEC cell. As shown in Table 2, the calculated resistance value of R_{ct1} for the $TiO_2/$
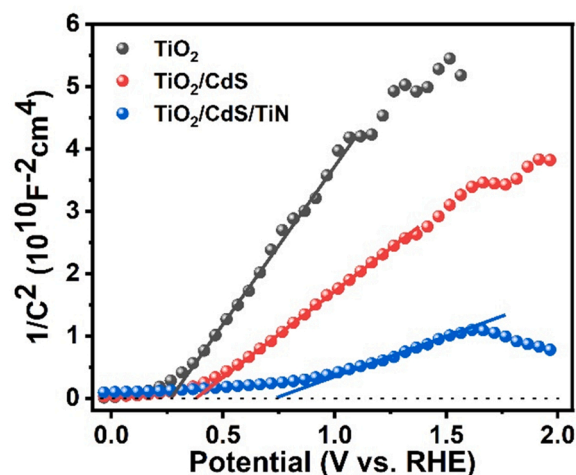
Fig. 9. M-S plots of the TiO_2, TiO_2/CdS and $TiO_2/CdS/TiN$ NRAs.

CdS/TiN NRA photoanode is 174 Ω, much lower than that (1606 Ω) of TiO_2 NRA photoanode, indicating that the type-II band structure which establishes between TiO_2 and CdS and the SPR effect of TiN can efficiently drive charge separation and transfer. Additionally, Bode phase plots can be used to determine recombination lifetime (τ_e) for the transfer electron according to $\tau_e = 1/(2\pi f_{max})$. Here, the characteristic maximum frequency (f_{max}) was obtained from the Bode phase plot in the low-frequency region [58,59]. As presented in Fig. 8b, the f_{max} of the $TiO_2/CdS/TiN$ NRA photoanode is the lowest, suggesting that the τ_e of $TiO_2/CdS/TiN$ NRA photoanode is the longest among the photoanodes. The calculated τ_e values of the TiO_2, TiO_2/CdS and $TiO_2/CdS/TiN$ NRA photoanodes are 61.0, 108.3, and 346.2 ms, respectively. The larger τ_e value indicates that the electron lifetime is increased and the recombination of the photoinduced charge carriers is efficiently suppressed, corresponding to a significantly enhanced PEC performance.

The electrochemically active surface area (ECSA) was used to further probe into the active sites of the $TiO_2/CdS/TiN$ NRA photoanode. It has been reported that the ECSA value of the photoelectrode is proportional to its double-layer capacitance (C_{dl}), which can be determined by the cyclic voltammetry (CV) measurements in the non-Faradaic region [35]. The C_{dl} value was obtained from the slope of the linearity of the plot of half current densities vs. scan rates. In the present work, the calculated C_{dl} values for the TiO_2/CdS and $TiO_2/CdS/TiN$ NRA photoanodes are 42.1 and 43.2 µF cm^{-2}, much larger than that (10.7 µF cm^{-2}) of pure TiO_2 NRA photoanode (Fig. S15). The experimental results demonstrate that the ECSA values of TiO_2/CdS and $TiO_2/CdS/TiN$ NRA photoanodes are almost same, demonstrating that the loading of TiN NPs does not decrease the active surface area of $TiO_2/CdS/TiN$ NRA photoanode. In addition, the ECSA value of TiO_2/CdS photoanode is much larger than that of TiO_2 NRA photoanode, clearly showing that 2D CdS nanosheets can provide large numbers of the active sites. Thus, the significant enhancement in ECSA value can provide large numbers of the active sites for $TiO_2/CdS/TiN$ NRA photoanode, leading to substantially enhanced PEC water splitting performances.

M-S plots were employed to further elucidate the mechanism for the enhanced PEC performance of the photoanodes. M-S measurements of
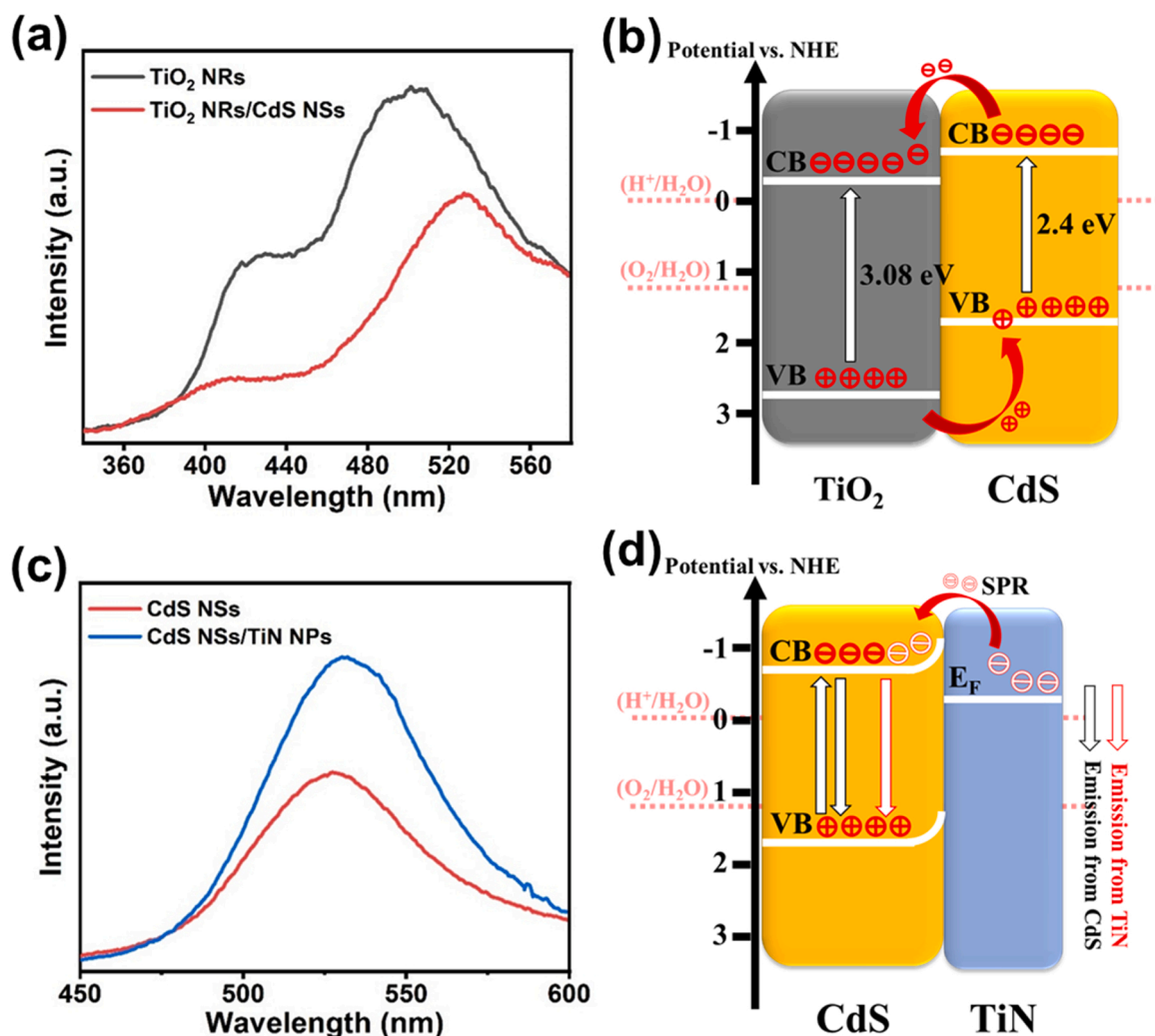
Fig. 10. (a) Rome temperature PL spectra of TiO_2 and TiO_2/CdS NRAs. (b) Photogenerated charge separation and transfer process between TiO_2 nanorods and CdS nanosheets. (c) Rome temperature PL spectra of CdS nanosheets and CdS/TiN heterostructures. (d) SPR-induced hot electron injection and charge separation process in CdS/TiN heterostructures.

the prepared photoanodes were conducted at an AC frequency of 1000 Hz under the bias of −1.0–1.0 V vs. Ag/AgCl and simulated sunlight irradiation, as presented in Fig. 9. It is evident that all the obtained photoanodes show conductive characteristics of n-type semiconductor with a positive slope, indicating that electrons were the majority carriers in the obtained photoanodes. As demonstrated in previous works, the flat-band potential of the semiconductor electrode can be obtained from the X-axis intercept of the M-S plot. Compared with the TiO_2 NRA photoanodes, the TiO_2/CdS and TiO_2/CdS/TiN NRA photoanodes show a positive shift of flat-band potential. However, the above LSV results show that the TiO_2/CdS/TiN NRA photoanode exhibits a cathodic shift of photocurrent onset potential compared to that of pure TiO_2 NRAs. Although opposite shift trend of photocurrent onset potential and flat-band potential is inconsistent with that of reported in some studies [60], this opposite shift trend has also been demonstrated in previous studies [57,61,62]. The reason for opposite shift trend of photocurrent onset potential and flat-band potential of TiO_2/CdS/TiN NRA photoanodes in this study is not clear and still needs to be study in future. A positive shift of flat-band potential suggests the decreased band edge bending of the heterostructure photoanodes. The decrease of the band edge bending of the heterostructure photoanodes can be attributed to the facilitated charge transfer in the electrode/electrolyte interface [57]. Moreover, the charge carrier density (N_D) of the as-prepared photoanodes can be estimated from the slope in the quasi-linear region of the

M-S plot according to the following equation [63,64]:

$$\frac{1}{C^2} = \frac{2}{\varepsilon_0 \varepsilon_r e N_D A_s^2} \left(V_{appl} - V_{FB} - \frac{kT}{e} \right) \tag{6}$$

$$N_D = \frac{2}{\varepsilon_0 \varepsilon_r e A_s^2} \left[\frac{d\left(1/C^2\right)}{dV} \right]^{-1} \tag{7}$$

The definitions of parameters in the above equations can be found in the previous reports [65,66]. According to the slope of M-S curves, the calculated N_D values for the TiO_2, TiO_2/CdS and TiO_2/CdS/TiN NRA photoanodes are 1.58×10^{19} cm^{-3}, 3.03×10^{19} cm^{-3} and 6.58×10^{19} cm^{-3}, respectively. The high carrier density for the TiO_2/CdS/TiN NRA photoanode demonstrates the effective charge separation caused by the type-II heterojunction within interface between the TiO_2 and CdS, as well as the injection of hot electrons of TiN NPs into CdS.

The room-temperature PL spectra were employed to attain an insight into the kinetic process of the photogenerated charges at the TiO_2/CdS and CdS/TiN interfaces in the obtained photoanodes. The PL spectra of the TiO_2 and TiO_2/CdS NRA photoanodes are shown in Fig. 10a. It can be found that the unmodified TiO_2 NRAs present a broad PL emission in the range of 350–550 nm with two emission peaks at ca. 410 and 500 nm, respectively. The emission peak at 410 nm originates from the near band-gap edge emission the rutile-phase TiO_2 NRAs and the
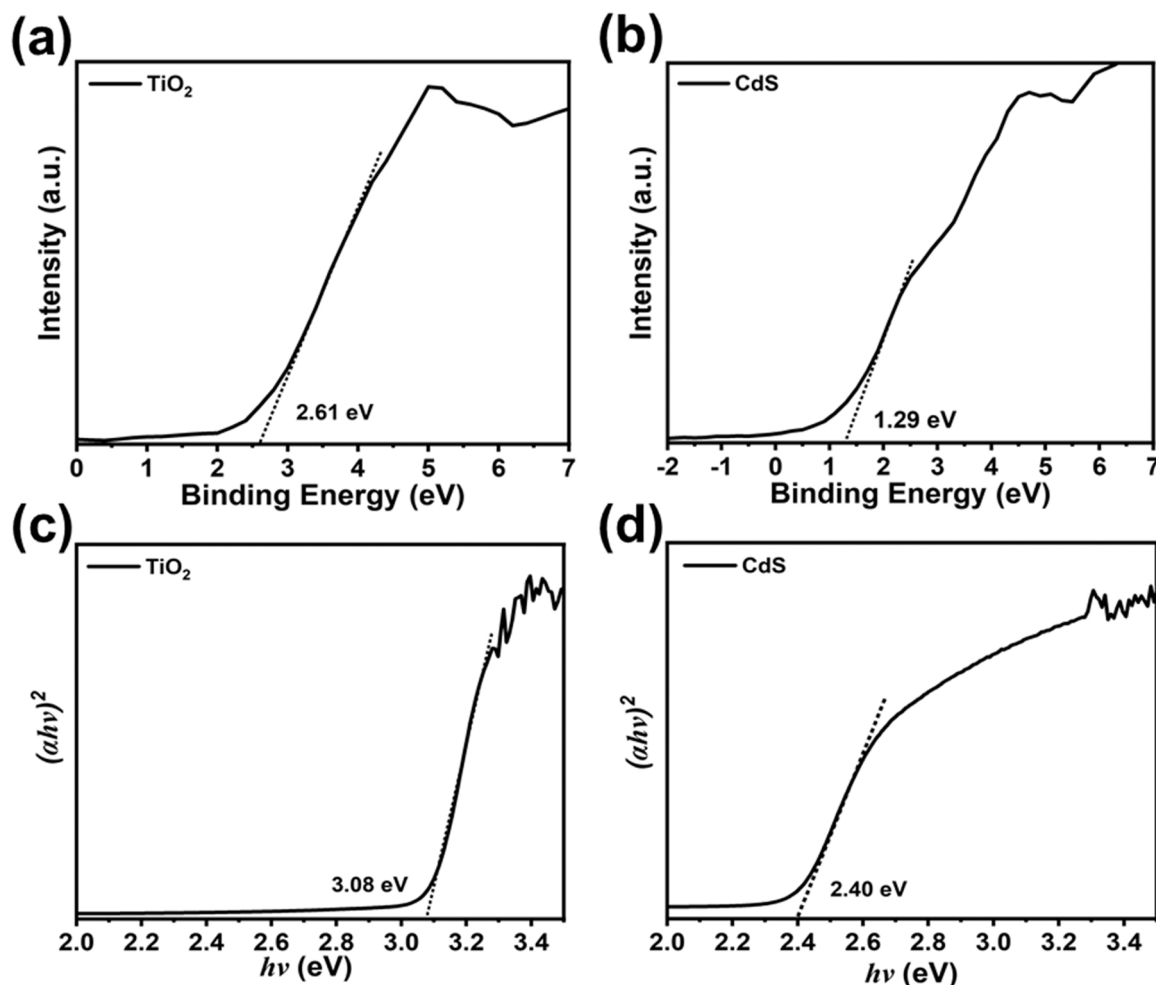
Fig. 11. Valence band XPS spectra for (a) TiO$_2$ and (b) CdS. Tauc plots of (c) TiO$_2$ and (d) CdS.

photoemission at 500 nm in visible region is caused by the defects in TiO$_2$ NRAs. Similar PL emission behaviour of the rutile-phase TiO$_2$ NRAs has been reported previously [45,67,68]. However, after CdS nanosheets were deposited on the TiO$_2$ NRAs, the emission intensity of two PL peaks in the TiO$_2$/CdS NRAs are obviously decreased, revealing that the photoexcited charges are separated effectively because of the type-II band structure between TiO$_2$ and CdS, as illustrated in Fig. 10b. It should be noted that TiO$_2$/CdS NRAs show a photoemission at 540 nm. This photoemission is attributed to band charge transitions of CdS. For the sake of further probing the SPR effect of TiN NPs, we tested and analyzed the PL properties of 2D CdS nanosheets and CdS/TiN heterostructures, as presented in Fig. 10c. Apparently, CdS nanosheets show a photoemission at around 540 nm originated from band charge transitions of CdS. However, the CdS/TiN heterostructures display significantly enhanced PL emission by comparison with that of the pristine CdS nanosheets. The enhanced PL emission intensity proves that recombination rate of photoinduced charges of CdS in the CdS/TiN heterostructure is increased, indicating that the numbers of photogenerated electrons in the CdS are augmented. Thus, the PL tests clearly reveal that TiN NPs are excited to generate hot electrons and then efficient inject them into CdS CB, as illustrated in Fig. 10d. This excitation and transport behavior for the hot electrons of TiN has been proven in previous studies [35,36,69]. Therefore, for the CdS/TiN heterostructure, the PL tests indisputably confirm that TiN NPs serve as an electron provider to inject their hot electron into the CdS CB, instead of serving as an electron receiver to extract the photo-generated electron from CdS. The above experimental results further confirm that type-II band alignment of the

TiO$_2$/CdS heterostructure and the SPR effect of the plasmonic TiN synergistically promote photogenerated charge carrier separation and transfer in the TiO$_2$/CdS/TiN NRA structure, resulting in substantially enhanced PEC H$_2$ production.

In order to rationally elucidate the photoexcited charge transfer pathway and improved PEC water splitting properties of the TiO$_2$/CdS/TiN NRA photoanode, the band alignment in as-prepared TiO$_2$/CdS/TiN heterostructure was determined by combining the valence band (VB) XPS and core-level XPS spectra (Fig. 11 and Fig. S2). In Fig. 11a and b, the VB maxima (VBM) values of pure TiO$_2$ and CdS are determined to be 2.61 and 1.29 eV, respectively. After modifying TiO$_2$ with CdS, the core-level XPS spectra show that the band energy of Ti 2p$_{3/2}$ changes from 458.7 to 458.4 eV (Fig. S2a) and the band energy of Cd 3d$_{5/2}$ changes from 405.1 to 405.2 eV (Fig. S2b). As displayed in Fig. 11c and d, the band gaps of pure TiO$_2$ and CdS are 3.08 and 2.40 eV, respectively. The band gaps are obtained from their UV–vis optical absorption spectra (Fig. 6a and S16). According to the experimental data of the heterojunction, the VB offset (VBO, ΔE_V) and CB offset (CBO, ΔE_c) between TiO$_2$ and CdS can be determined by the following equations [70]:

$$\Delta E_{V(TiO2/CdS)} = (E_{Cd3d5/2} - E_{VBM})_{CdS} - (E_{Ti2p3/2} - E_{VBM})_{TiO2} - (E_{Cd3d5/2} - E_{Ti2p3/2})_{TiO2/CdS} \tag{8}$$

$$\Delta E_{C(TiO2/CdS)} = E_{g\ CdS} - E_{g\ TiO2} + \Delta E_{V(TiO2/CdS)} \tag{9}$$

The calculated ΔE_V and ΔE_c between TiO$_2$ and CdS in heterojunction are 0.92 and 0.24 eV, respectively. These results demonstrate that both the CB and VB positions of CdS are higher than those of TiO$_2$, resulting in the establishment of a type-II band alignment between the interface of
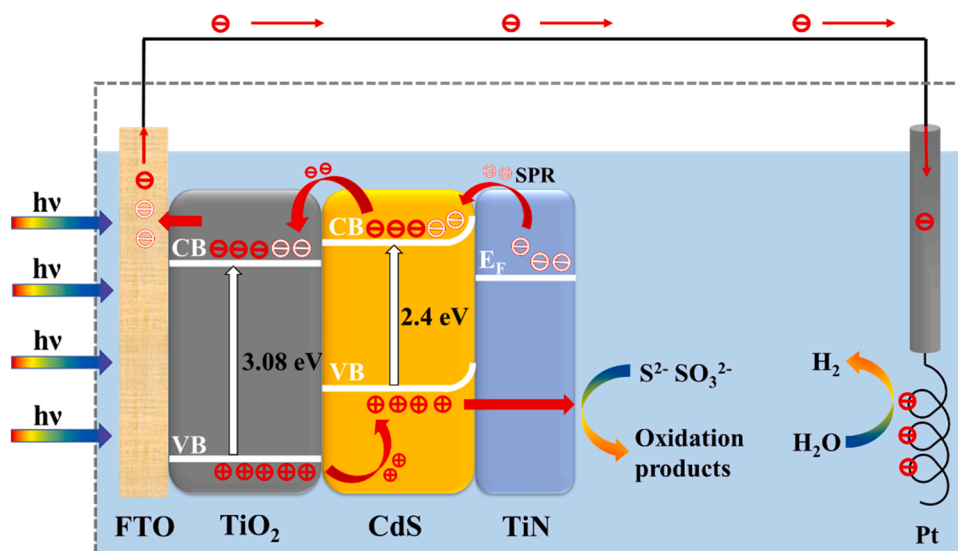
Fig. 12. (a) Schematic illustration of photogenerated charge transfer process in the TiO_2/CdS/TiN NRA photoanode.

TiO_2 and CdS. The established type-II band alignment facilitates the separation and transfer of photogenerated carries from the CB of CdS to that of TiO_2.

According to the above measurements and analysis, a possible photogenerated charge transfer mechanism for the TiO_2/CdS/TiN heterostructure under solar light illumination is illustrated in Fig. 12. When the as-prepared ternary heterostructure is irradiated by simulated sunlight, the TiO_2 and CdS can produce photogenerated electron and hole pairs. Meanwhile, the plasmonic TiN NPs can be excited to produce hot electrons under the irradiation of simulated sunlight. The SPR effect of TiN NPs will inject their hot electrons into CdS CB. Then, the hot electrons inject into CdS CB and the photogenerated electrons of CdS move to TiO_2 CB. Finally, the photoexcited electrons of the TiO_2 and CdS together with hot electrons of TiN migrate to counter electrode Pt wire via an external circuit to generated H_2 through water splitting. Meanwhile, the photogenerated holes of TiO_2 transport from its VB to that of CdS, followed by migrating to the heterostructure surface to react with Na_2S and Na_2SO_3 in the electrolyte. Thus, the remarkably improved PEC H_2 production of ternary TiO_2/CdS/TiN NRA photoanode is contributed to SPR-induced hot electron injection of TiN NPs and the efficient charge separation.

4. Conclusions

A novel ternary TiO_2/CdS/TiN NRA photoanode integrating with type-II band arrangement and nonmetal plasmonic sensitizer has been successfully constructed by successively modifying with 2D CdS nanosheets and TiN NPs for the first time. 2D CdS nanosheets with large surface area not only remarkably boost visible light absorption, but also expand the contact area with TiO_2 to construct type-II band structure. The type-II band structure formed at the TiO_2 and CdS interface can accelerate the charge separation and transfer efficiently. Additionally, 2D CdS nanosheets offer more sites to incorporate TiN NPs, further improving the visible light absorption. Moreover, the nonmental plasmonic TiN NPs produce numerous hot electrons to inject into CdS CB driven by the SPR effect. These synergistic effects improve the ability to harvest solar light and facilitate charge transport and separation in the TiO_2/CdS/TiN NRA photoanode, resulting in a substantially boosted photocurrent density of 4.5 mA cm^{-2} under bias-free simulated sunlight illumination. Moreover, the PEC H_2 generation rate of the TiO_2/CdS/ TiN NRA photoanode is 129.6 µmol cm^{-2} h^{-1}, which is 4.2 times higher than that of the pure TiO_2 NRA photoanode. This present study opens a new way for integrating type-II band structure and nonmetal plasmonic

sensitizer into a single photoanode to achieve efficient conversion of solar energy into chemical fuels.

CRediT authorship contribution statement

Jianan Li: Data curation, Investigation, Writing – original draft. **Lijuan Wang:** Conceptualization, Methodology. **Wenzhong Wang:** Supervision, Writing – review & editing. **Xinglin Jia:** Data curation. **Yuanyuan Zhang:** Data curation. **Hang Yang:** Investigation, Resources. **Yujie Li:** Formal analysis. **Qing Zhou:** Writing – review & editing, Supervision.

Declaration of Competing Interest

The authors declare that they have no known competing financial interests or personal relationships that could have appeared to influence the work reported in this paper.

Data Availability

No data was used for the research described in the article.

Acknowledgments

Appendix A. Supporting information

Supplementary data associated with this article can be found in the online version at doi:10.1016/j.apcatb.2023.122833.

References

[1] B. Luo, D.L. Ye, L.Z. Wang, Recent progress on integrated energy conversion and storage systems, Adv. Sci. 4 (2017), 170010, https://doi.org/10.1002/advs.201700104.

[2] Q. Zeng, Y.Q. Lai, L.X. Jiang, F.Y. Liu, X.J. Hao, L.Z. Wang, M.A. Green, Integrated photorechargeable energy storage system: next-generation power source driving the future, Adv. Energy Mater. 10 (2020) 1903930, https://doi.org/10.1002/aenm.201903930.

[3] H. Guan, S. Zhang, X. Cai, Q. Gao, X. Yu, X. Zhou, F. Peng, Y. Fang, S. Yang, CdS@ Ni₃S₂ core-shell nanorod arrays on nickel foam: a multifunctional catalyst for efficient electrochemical catalytic, photoelectrochemical and photocatalytic H2 production reaction, J. Mater. Chem. A 7 (2019) 2560–2574, https://doi.org/ 10.1039/C8TA08837C.

[4] S. Cho, G. Yim, J. Park, H. Jang, Surfactant-free one-pot synthesis of Au-TiO₂ core-shell nanostars by inter-cation redox reaction for photoelectrochemical water splitting, Energy Convers. Manag. 252 (2022), 115038, https://doi.org/10.1016/j. enconman.2021.115038.

[5] I. Cho, Z. Chen, A. Forman, D. Kim, P. Rao, T. Jaramillo, X. Zheng, Branched TiO₂ nanorods for photoelectrochemical hydrogen production, Nano Lett. 11 (2011) 4978–4984, https://doi.org/10.1021/nl2029392.

[6] Z. Kang, H. Si, S. Zhang, J. Wu, Y. Sun, Q. Liao, Z. Zhang, Y. Zhang, Interface engineering for modulation of charge carrier behavior in ZnO photoelectrochemical water splitting, Adv. Funct. Mater. 29 (2019) 1808032, https://doi.org/10.1002/adfm.201808032.

[7] C.Y. Shao, A.S. Malik, J.F. Han, D. Li, M. Dupuis, X. Zong, C. Lia, Oxygen vacancy engineering with flame heating approach towards enhanced photoelectrochemical water oxidation on WO₃ photoanode, Nano Energy 77 (2020), 105190, https://doi. org/10.1016/j.nanoen.2020.105190.

[8] W.Y. Jiang, Y. An, Z.Y. Wang, M.R. Wang, X.L. Bao, L.R. Zheng, H.F. Cheng, P. Wang, Y.Y. Liu, Z.K. Zheng, Y. Dai, B.B. Huang, Stress-induced BiVO₄ photoanode for enhanced photoelectrochemical performance, Appl. Catal. B 304 (2022), 121012, https://doi.org/10.1016/j.apcatb.2021.121012.

[9] Y.J. Jeong, S.W. Hwang, S. Chaikasetsin, H.S. Han, I.S. Cho, Dual textured BiVO₄/ Sb:SnO₂ heterostructure for enhanced photoelectrochemical Water-splitting, Chem. Eng. J. 435 (2022), 135183, https://doi.org/10.1016/j.cej.2022.135183.

[10] M.H. Wu, Y.X. Wang, Y. Xu, J. Ming, M. Zhou, R. Xu, Q. Fu, Y. Lei, Self-supported Bi₂MoO₆ Nanowall for Photoelectrochemical Water Splitting, ACS Appl. Mater. Interfaces 9 (2017) 23647–23653, https://doi.org/10.1021/acsami.7b03801.

[11] A. Fujishima, K. Honda, Electrochemical photolysis of water at a semiconductor electrode, Nature 238 (1972) 37–38, https://doi.org/10.1038/238037a0.

[12] C. Peng, W. Wang, W. Zhang, Y. Liang, L. Zhuo, Surface plasmon-driven photoelectrochemical water splitting of TiO₂ nanowires decorated with Ag nanoparticles under visible light illumination, Appl. Surf. Sci. 420 (2017) 286–295, https://doi.org/10.1016/j.apsusc.2017.05.101.

[13] S. Franz, H. Arab, G.L. Chiarello, M. Bestetti, E. Selli, Single-step preparation of large area TiO₂ photoelectrodes for water splitting, Adv. Energy Mater. (2020) 2000652, https://doi.org/10.1002/aenm.202000652.

[14] Y. Pu, G. Wang, K. Chang, Y. Ling, Y. Lin, B. Fitzmorris, C. Liu, X. Lu, Y. Tong, J. Zhang, Y. Hsu, Y. Li, Au nanostructure-decorated TiO₂ nanowires exhibiting photoactivity across entire UV–visible region for photoelectrochemical water splitting, Nano Lett. 13 (2013) 3817–3823, https://doi.org/10.1021/nl4018385.

[15] C. Hao, W. Wang, R. Zhang, B. Zou, H. Shi, Enhanced photoelectrochemical water splitting with TiO₂@Ag₂O nanowire arrays via p-n heterojunction formation, Sol. Energ. Mat. Sol. C. 174 (2018) 132–139, https://doi.org/10.1016/j. solmat.2017.08.033.

[16] M. Elbakkay, W.M.A. El Rouby, S.I. El-Dek, A.A. Farghali, S- TiO₂/S-reduced graphene oxide for enhanced photoelectrochemical water splitting, Appl. Surf. Sci. 439 (2018) 1088–1102, https://doi.org/10.1016/j.apsusc.2018.01.070.

[17] P. Liu, X. Liu, X. Huo, Y. Tang, J. Xu, H. Ju, TiO₂-BiVO₄ heterostructure to enhance photoelectrochemical efficiency for sensitive aptasensing, ACS Appl. Mater. Interfaces 9 (2017) 27185–27192, https://doi.org/10.1021/acsami.7b07047.

[18] L. Yang, W. Wang, H. Zhang, S. Wang, M. Zhang, G. He, J. Lv, K. Zhu, Z. Sun, Electrodeposited Cu₂O on the {101} facets of TiO₂ nanosheet arrays and their enhanced photoelectrochemical performance, Sol. Energ. Mat. Sol. C. 165 (2017) 27–35, https://doi.org/10.1016/j.solmat.2017.02.026.

[19] B.Y. Cheng, J.S. Yang, H.W. Cho, J.J. Wu, Fabrication of an efficient BiVO₄-TiO₂ heterojunction photoanode for photoelectrochemical water oxidation, ACS Appl. Mater. Interfaces 8 (2016) 20032–20039, https://doi.org/10.1021/ acsami.6b05489.

[20] G.J. Ai, H.X. Li, S.P. Liu, R. Mo, J.X. Zhong, Solar water splitting by TiO₂/CdS/Co-Pi nanowire array photoanode enhanced with Co-Pi as hole transfer relay and CdS as light absorber, Adv. Funct. Mater. 25 (2015) 5706–5713, https://doi.org/ 10.1002/adfm.201502461.

[21] L. Yao, W. Wang, L. Wang, Y. Liang, J. Fu, H. Shi, Chemical bath deposition synthesis of TiO₂/Cu₂O core/shell nanowire arrays with enhanced photoelectrochemical water splitting for H₂ evolution and photostability, Int. J. Hydrog. Energy 43 (2018) 15907–15917, https://doi.org/10.1016/j. ijhydene.2018.06.127.

[22] Z. Braiek, J. Ben Naceur, F. Jrad, I. Ben Assaker, R. Chtourou, Novel synthesis of graphene oxide/In₂S₃/TiO₂ NRs heterojunction photoanode for enhanced photoelectrochemical (PEC) performance, Int. J. Hydrog. Energy 47 (2022) 3655–3666, https://doi.org/10.1016/j.ijhydene.2021.10.268.

[23] Z. Bai, X. Yan, Y. Li, Z. Kang, S. Cao, Y. Zhang, 3D-branched ZnO/CdS nanowire arrays for solar water splitting and the service safety research, Adv. Energy Mater. 6 (2016) 1501459, https://doi.org/10.1002/aenm.201501459.

[24] Y.Y. Zhang, H.W. Hu, W.W. Kang, G.J. Qiu, R.Y. Liang, L.F. Deng, H.R. Yuan, Enhancing hydrogen evolution by photoelectrocatalysis of water splitting over a CdS flowers-loaded TiO₂ nanotube array film on the Ti foil substrate, Ceram. Int. 46 (2020) 17606–17613, https://doi.org/10.1016/j.ceramint.2020.04.062.

[25] Q. Li, B. Guo, J. Yu, J. Ran, B. Zhang, H. Yan, J.R. Gong, Highly efficient visible-light-driven photocatalytic hydrogen production of CdS-cluster-decorated graphene nanosheets, J. Am. Chem. Soc. 133 (2011) 10878–10884, https://doi. org/10.1021/ja2025454.

[26] J. Yu, Y. Yu, P. Zhou, W. Xiao, B. Cheng, Morphology-dependent photocatalytic H₂-production activity of CdS, Appl. Catal. B 156–157 (2014) 184–191, https://doi. org/10.1016/j.apcatb.2014.03.013.

[27] L. Wang, W. Wang, Y. Chen, L. Yao, X. Zhao, H. Shi, M. Cao, Y. Liang, Heterogeneous p-n junction CdS/Cu₂O nanorod arrays: synthesis and superior visible-light-driven photoelectrochemical performance for hydrogen evolution, ACS Appl. Mater. Interfaces 10 (2018) 11652–11662, https://doi.org/10.1021/ acsami.7b19530.

[28] T. Yu, W. Cheng, K. Chao, S. Lu, ZnFe₂O₄ decorated CdS nanorods as a highly efficient, visible light responsive, photochemically stable, magnetically recyclable photocatalyst for hydrogen generation, Nanoscale 5 (2013) 7356–7360, https:// doi.org/10.1039/C3NR02658B.

[29] S. Zhang, Z. Liu, W. Yan, Z. Guo, M. Ruan, Decorating non-noble metal plasmonic Al on a TiO₂/Cu₂O photoanode to boost performance in photoelectrochemical water splitting, Chin. J. Catal. 41 (2020) 1884–1893, https://doi.org/10.1016/ S1872-2067(20)63637-3.

[30] P. Zhang, T. Wang, J. Gong, Mechanistic understanding of the plasmonic enhancement for solar water splitting, Adv. Mater. 27 (2015) 5328–5342, https:// doi.org/10.1002/adma.201500888.

[31] C. Clavero, Plasmon-induced hot-electron generation at nanoparticle/metal-oxide interfaces for photovoltaic and photocatalytic devices, Nat. Photonics 8 (2014) 95–103, https://doi.org/10.1038/nphoton.2013.238.

[32] H. Li, H. Liu, F. Wang, G. Li, X. Wang, Z. Tang, Hot electron assisted photoelectrochemical water splitting from Au-decorated ZnO@ TiO₂ nanorods array, Nano Res 15 (2022) 5824–5830, https://doi.org/10.1007/s12274-022-4203-z.

[33] R. Salimi, A.A. Sabbagh Alvani, H. Sameie, D. Poelman, F. Rosei, Designing 1D plasmonic Ag/CuWO₄ nanocomposite for enhancing visible-light photoelectrochemical performance, J. Electrochem. Soc. 169 (2022), 086503, https://doi.org/10.1149/1945-7111/ac88f7.

[34] G.Y. Qiu, A. Thakur, C. Xu, S.P. Ng, Y.J. Lee, C.M.L. Wu, Detection of glioma-derived exosomes with the biotinylated antibody-functionalized titanium nitride plasmonic biosensor, Adv. Funct. Mater. 29 (2019) 1806761, https://doi.org/ 10.1002/adfm.201806761.

[35] Y. Li, J. Wang, Y. Fan, H. Sun, W. Hua, H. Liu, B. Wei, Plasmonic TiN boosting nitrogen-doped TiO₂ for ultrahigh efficient photoelectrochemical oxygen evolution, Appl. Catal. B 246 (2019) 21–29, https://doi.org/10.1016/j. apcatb.2019.01.044.

[36] Y. Liu, T. Zhu, M. Lin, Y. Liang, J. Fu, W. Wang, Nonmetal plasmonic TiN nanoparticles significantly boost photoelectrochemical performance for hydrogen evolution of CdS nanoroad array photoanode, Renew. Energ. 180 (2021) 1290–1299, https://doi.org/10.1016/j.renene.2021.09.050.

[37] J.P. Enríquez, X. Mathew, Influence of the thickness on structural, optical and electrical properties of chemical bath deposited CdS thin films, Sol. Energ. Mat. Sol. C. 76 (2003) 313–322, https://doi.org/10.1016/S0927-0248(02)00283-0.

[38] T. Lan, X.L. Tang, B. Fultz, Phonon anharmonicity of rutile TiO₂ studied by Raman spectrometry and molecular dynamics simulations, Phys. Rev. B 85 (2012), 094305, https://doi.org/10.1103/PhysRevB.85.094305.

[39] A. Valour, M.A.U. Higuita, N.C. Monteiro, S. Reynaud, M. Hochedel, D. Jamon, C. Donnet, Y. Jourlin, Micro-nanostructured TiN thin film: synthesis from a photo-patternable TiO₂ Sol-Gel coating and rapid thermal nitridation, J. Phys. Chem. C. 124 (2020) 25480–25488, https://doi.org/10.1021/acs.jpcc.0c07157.

[40] P. Xue, Q. Li, W. Gong, Z. Sun, H. Wang, K. Zhu, C. Guo, G. Hong, W. Xu, J. Sun, Y. Yao, Z. Liu, Structure-induced partial phase transformation endows hollow TiO₂/TiN heterostructure fibers stacked with nanosheet arrays with extraordinary sodium storage performance, J. Mater. Chem. A 9 (2021) 12109–12118, https:// doi.org/10.1039/D1TA01729B.

[41] L. Ma, L. Yu, J. Liu, Y. Su, S. Li, X. Zang, T. Meng, S. Zhang, J. Song, J. Wang, X. Zhao, Z. Cui, N. Wang, Y. Zhao, Construction of Ti₄O₇/TiN/carbon microdisk sulfur host with strong polar N-Ti-O bond for ultralong life lithium-sulfur battery, Energy Stor, Mater 44 (2022) 180–189, https://doi.org/10.1016/j. ensm.2021.09.024.

[42] J. Yu, L. Zhang, Z. Zheng, J. Zhao, Synthesis and characterization of phosphated mesoporous titanium dioxide with high photocatalytic activity, Chem. Mater. 15 (2003) 2280–2286, https://doi.org/10.1021/cm0340781.

[43] L.B. Wang, B. Cheng, L.Y. Zhang, J.G. Yu, In situ irradiated XPS investigation on S-scheme TiO₂@ZnIn₂S₄ photocatalyst for efficient photocatalytic CO₂ reduction, Small 17 (2021) 2103447, https://doi.org/10.1002/smll.202103447.

[44] F. Ning, M. Shao, S. Xu, Y. Fu, R. Zhang, M. Wei, D.G. Evans, X. Duan, TiO₂/ graphene/NiFe-layered double hydroxide nanorod array photoanodes for efficient photoelectrochemical water splitting, Energy Environ. Sci. 9 (2016) 2633–2643, https://doi.org/10.1039/C6EE01092J.

[45] K. Jiang, W. Wang, J. Wang, T. Zhu, L. Yao, Y. Cheng, Y. Wang, Y. Liang, J. Fu, Cu₂O nanoparticles sensitize TiO₂/CdS nanowire arrays to prolong charge carrier lifetime and highly enhance unassisted photoelectrochemical hydrogen generation with 4.3% efficiency, Dalton Trans. 49 (2020) 9282–9293, https://doi.org/ 10.1039/D0DT01643H.

[46] S.L. Shinde, S. Ishii, T.D. Dao, R.P. Sugavaneshwar, T. Takei, K.K. Nanda, T. Nagao, Enhanced solar light absorption and photoelectrochemical conversion using TiN nanoparticle-incorporated C₃N₄-C dot sheets, ACS Appl. Mater. Interfaces 10 (2018) 2460–2468, https://doi.org/10.1021/acsami.7b15066.

[47] G.S. Shanker, G.B. Markad, M. Jagadeeswararao, U. Bansode, A. Nag, Colloidal nanocomposite of TiN and N-doped few-layer graphene for plasmonics and electrocatalysis, ACS Energy Lett. 2 (2017) 2251–2256, https://doi.org/10.1021/ acsenergylett.7b0074.

[48] Z. Xie, X. Liu, W. Wang, X. Wang, C. Liu, Q. Xie, Z. Li, Z. Zhang, Enhanced photoelectrochemical and photocatalytic performance of TiO$_2$ nanorod arrays/CdS quantum dots by coating TiO$_2$ through atomic layer deposition, Nano Energy 11 (2015) 400–408, https://doi.org/10.1016/j.nanoen.2014.11.024.

[49] S. Sadhasivam, A. Gunasekaran, N. Anbarasan, N. Mukilan, K. Jeganathan, CdS and CdSe nanoparticles activated 1D TiO$_2$ heterostructure nanoarray photoelectrodes for enhanced photoelectrocatalytic water splitting, Int. J. Hydrog. Energy 46 (2021) 26381–26390, https://doi.org/10.1016/j.ijhydene.2021.05.144.

[50] S.S.M. Bhat, S.A. Pawar, D. Potphode, C.-K. Moon, J.M. Suh, C. Kim, S. Choi, D. S. Patil, J.-J. Kim, J.C. Shin, H.W. Jang, Substantially enhanced photoelectrochemical performance of TiO$_2$ nanorods/CdS nanocrystals heterojunction photoanode decorated with MoS$_2$ nanosheets, Appl. Catal. B 259 (2019), 118102, https://doi.org/10.1016/j.apcatb.2019.118102.

[51] P. Lv, W. Fu, H. Yang, H. Sun, Y. Chen, J. Ma, X. Zhou, L. Tian, W. Zhang, M. Li, H. Yao, D. Wu, Simple synthesis method of Bi$_2$S$_3$/CdS quantum dots cosensitized TiO$_2$ nanotubes array with enhanced photoelectrochemical and photocatalytic activity, CrystEngComm 15 (2013) 7548–7555, https://doi.org/10.1039/C3CE40863A.

[52] P. Lv, W. Fu, Y. Mu, H. Sun, S. Su, Y. Chen, H. Yao, D. Ding, T. Liu, J. Wang, H. Yang, Photoelectrochemical property of CdS and PbS cosensitized on the TiO$_2$ array by novel successive ionic layer adsorption and reaction method, J. Alloy. Compd. 621 (2015) 30–34, https://doi.org/10.1016/j.jallcom.2014.09.172.

[53] J. Zhu, Y. Cheng, W. Zhang, J. Zhao, Q. Sun, X. Hu, H. Miao, Interfacial charge and surface defect regulation for high-efficiency CdIn$_2$S$_4$-based photoanodes, Appl. Surf. Sci. 601 (2022), 154188, https://doi.org/10.1016/j.apsusc.2022.154188.

[54] V. González-Pedro, I. Zarazua, E.M. Barea, F. Fabregat-Santiago, E. de la Rosa, I. Mora-Seró, S. Giménez, Panchromatic solar-to-H2 conversion by a hybrid quantum dots-dye dual absorber tandem device, J. Phys. Chem. C. 118 (2014) 891–895, https://doi.org/10.1021/jp4109893.

[55] R. Raja, P. Sudhagar, A. Devadoss, C. Terashima, L.K. Shrestha, K. Nakata, R. Jayavel, K. Ariga, A. Fujishima, Pt-free solar driven photoelectrochemical hydrogen fuel generation using 1T MoS$_2$ co-catalyst assembled CdS QDs/TiO$_2$ photoelectrode, Chem. Commun. 51 (2015) 522–525, https://doi.org/10.1039/C4CC07304E.

[56] A. Naldoni, U. Guler, Z.X. Wang, M. Marelli, F. Malara, X.G. Meng, L.V. Besteiro, A. O. Govorov, A.V. Kildishev, A. Boltasseva, V.M. Shalaev, Using a CeO$_2$ quantum dot hole extraction-layer for enhanced solar water splitting activity of BiVO$_4$ photoanodes, Chem. Eng. J. 450 (2022) 137917, https://doi.org/10.1002/adom.201601031.

[57] T.S. Zhou, J.C. Wang, S. Chen, J. Bai, J.H. Li, Y. Zhang, L.S. Li, L.G. Xia, M. Rahim, Q.J. Xu, B.X. Zhou, Bird-nest structured ZnO/TiO$_2$ as a direct Z-scheme photoanode with enhanced light harvesting and carriers kinetics for highly efficient and stable photoelectrochemical water splitting, Appl. Catal. B 267 (2020), 118599, https://doi.org/10.1016/j.apcatb.2020.118599.

[58] J. Wan, L. Tao, B. Wang, J. Zhang, H. Wang, P.D. Lund, A facile method to produce TiO$_2$ nanorods for high-efficiency dye solar cells, J. Power Sources 438 (2019), 227012, https://doi.org/10.1016/j.jpowsour.2019.227012.

[59] S. Zhang, Z. Liu, M. Ruan, Z. Guo, L. E, W. Zhao, D. Zhao, X. Wu, D. Chen, Enhanced piezoelectric-effect-assisted photoelectrochemical performance in ZnO modified with dual cocatalysts, Appl. Catal. B 262 (2020), 118279, https://doi.org/10.1016/j.apcatb.2019.118279.

[60] H.M. Zhang, D.F. Li, W.J. Byun, X.L. Wang, T.J. Shin, H.Y. Jeong, H.X. Han, C. Li, J. S. Lee, Gradient tantalum-doped hematite homojunction photoanode improves both photocurrents and turn-on voltage for solar water splitting, Nat. Commun. 11 (2020) 4622, https://doi.org/10.1038/s41467-020-18484-8.

[61] R.K. Zhang, M.F. Shao, S.M. Xu, F.Y. Ning, L. Zhou, M. Wei, Photo-assisted synthesis of zinc-iron layered double hydroxides/TiO$_2$ nanoarrays toward highly-efficient photoelectrochemical water splitting, Nano Energy 33 (2017) 21–28, https://doi.org/10.1016/j.nanoen.2017.01.020.

[62] H. Xu, H.W. Chen, S.C. Chen, K. Wang, X.T. Wang, Fabrication of In$_2$O$_3$/In$_2$S$_3$ heterostructures for enhanced photoelectrochemical performance, Int. J. Hydrog. Energy 46 (2021) 32445–32454, https://doi.org/10.1016/j.ijhydene.2021.07.085.

[63] K. Tian, L. Wu, T. Han, L. Gao, P. Wang, H. Chai, J. Jin, Dual modification of BiVO$_4$ photoanode by rare earth element neodymium doping and further NiFe$_2$O$_4$ co-catalyst deposition for efficient photoelectrochemical water oxidation, J. Alloy. Compd. 923 (2022), 166352, https://doi.org/10.1016/j.jallcom.2022.166352.

[64] H. Zhang, X. Bai, Photocatalytic production of hydrogen peroxide over Z-scheme Mn$_3$O$_4$/Co$_9$S$_8$ with p-n heterostructure, Appl. Catal. B 298 (2021), 120516, https://doi.org/10.1016/j.apcatb.2021.120516.

[65] T.Y. Zhu, Y.J. Liang, Y.N. Wang, J. Wang, W.Z. Wang, J.L. Fu, L.Z. Yao, Y. Cheng, H.S. Han, P-type β-Ni(OH)$_2$ nanoparticles sensitize CdS nanorod array photoanode to prolong charge carrier lifetime and highly improve bias-free visible-light-driven H$_2$ evaluation, Appl. Catal. B 271 (2020), 118945, https://doi.org/10.1016/j.apcatb.2020.118945.

[66] Y. Lu, Z. Wei, N.P. Salke, L. Yu, H. Yan, Enhanced electron transport in rutile TiO$_2$ nanowires via H$_2$S-assisted incorporation of dissolved silicon for solar-driven water splitting, Appl. Catal. B 244 (2019) 767–772, https://doi.org/10.1016/j.apcatb.2018.12.003.

[67] Y. Lei, L. Zhang, G. Meng, G. Li, X. Zhang, C. Liang, W. Chen, S. Wang, Preparation and photoluminescence of highly ordered TiO$_2$ nanowire arrays, Appl. Phys. Lett. 78 (2001) 1125–1127, https://doi.org/10.1063/1.1350959.

[68] J. Yu, H. Yu, B. Cheng, X. Zhao, J. Yu, W. Ho, The effect of calcination temperature on the surface microstructure and photocatalytic activity of TiO$_2$ thin films prepared by liquid phase deposition, J. Phys. Chem. B 107 (2003) 13871–13879, https://doi.org/10.1021/jp036158y.

[69] A. Naldoni, U. Guler, Z.X. Wang, M. Marelli, F. Malara, X.G. Meng, L.V. Besteiro, A. O. Govorov, A.V. Kildishev, A. Boltasseva, V.M. Shalaev, Broadband hot-electron collection for solar water splitting with plasmonic titanium nitride, Adv. Opt. Mater 5 (2017) 1601031–1601041, https://doi.org/10.1002/adom.201770079.

[70] L.Z. Yao, W.Z. Wang, Y.J. Liang, J.L. Fu, H.L. Shi, Plasmon-enhanced visible light photoelectrochemical and photocatalytic activity of gold nanoparticle-decorated hierarchical TiO$_2$/Bi$_2$WO$_6$ nanorod arrays, Appl. Surf. Sci. 469 (2019) 829–840, https://doi.org/10.1016/j.apsusc.2018.11.031.